A Unified RANS-LES Model: Computational Development, Accuracy and Cost

Harish Gopalan[a], Stefan Heinz[b,*], Michael K. Stöllinger[a]

[a]Mechanical Engineering Department, University of Wyoming, 1000 E. University Avenue, Laramie, WY 82071, USA
[b]Department of Mathematics, University of Wyoming, 1000 E. University Avenue, Laramie, WY 82071, USA

Abstract

Large eddy simulation (LES) is computationally extremely expensive for the investigation of wall-bounded turbulent flows at high Reynolds numbers. A way to reduce the computational cost of LES by orders of magnitude is to combine LES equations with Reynolds-averaged Navier-Stokes (RANS) equations used in the near-wall region. A large variety of such hybrid RANS-LES methods are currently in use such that there is the question of which hybrid RANS-LES method represents the optimal approach. The properties of an optimal hybrid RANS-LES model are formulated here by taking reference to fundamental properties of fluid flow equations. It is shown that unified RANS-LES models derived from an underlying stochastic turbulence model have the properties of optimal hybrid RANS-LES models. The rest of the paper is organized in two parts. First, *a priori* and *a posteriori* analyses of channel flow data are used to find the optimal computational formulation of the theoretically derived unified RANS-LES model and to show that this computational model, which is referred to as linear unified model (LUM), does also have all the properties of an optimal hybrid RANS-LES model. Second, *a posteriori* analyses of channel flow data are used to study the accuracy and cost features of the LUM. The following conclusions are obtained. (i) Compared to RANS, which require evidence for their predictions, the LUM has the significant advantage that the quality of predictions is relatively independent of the RANS model applied. (ii) Compared to LES, the significant advantage of the LUM is a cost reduction of high-Reynolds number simulations by a factor of $0.07\,Re^{\,0.46}$. For coarse grids, the LUM has a significant accuracy advantage over corresponding LES. (iii) Compared to other usually applied hybrid RANS-LES models, it is shown that the LUM provides significantly improved predictions.

Keywords: Stochastic turbulence model, RANS, LES, Unified RANS-LES models, Channel flow application

---

1. Introduction

The use of direct numerical simulation (DNS) to numerically integrate the basic equations of fluid mechanics and thermodynamics is extremely helpful for studying the fundamental mechanisms of turbulent flows, but the computational cost of DNS do not allow investigations of complex engineering and environmental flows. For example, the

---

[*] Corresponding author. Tel.: 1 307 766 4203; fax.: 1 307 766 6838

Email addresses: `hgopalan@uwyo.edu` (Harish Gopalan), `heinz@uwyo.edu` (Stefan Heinz), `MStoell@uwyo.edu` (Michael K. Stöllinger)

number of grid points N required to perform DNS of turbulent channel flow scales with the Reynolds number Re according to $N \sim Re^{2.7}$ [1, 2]. A solution for this cost problem requires the use of modeling assumptions for at least a part of the spectrum of turbulent motions.

There are two ways that have been used to address this issue. The first way, deterministic [2–9] or stochastic [10–17] large eddy simulation (LES) methods, applies modeling assumptions to small-scale turbulent motions while the energetic large scale structures are resolved. The second way, deterministic [2, 18, 19] or stochastic [2, 20–22], Reynolds-averaged Navier-Stokes (RANS) methods, applies modeling assumptions to all the scales of motion. The use of LES methods is much cheaper than DNS regarding the simulation of complex free shear flows: the total number of grid points required scales as $N \sim Re^{0.4}$ [23]. However, for wall-bounded flows the cost of fully resolved LES scales as $N \sim Re^{1.76}$ [24, 25], which is comparable to DNS. Therefore, it is very expensive to use LES for simulations of complex wall-bounded engineering and environmental flows at high Reynolds numbers. The use of RANS methods can reduce the computational cost of complex wall-bounded flow simulations. The number of grid points required to perform RANS simulations of wall-bounded flows is independent of the Reynolds number along the streamwise and spanwise directions and scales as $N \sim \ln Re$ along the wall normal direction [2]. However, there are two issues associated with the use of RANS models for turbulent flow simulations. First, the accuracy of numerical predictions depends on the choice of the RANS model ($k - \epsilon$, $k - \omega$, etc.) and flow considered (separated flows, swirling flows, etc.) [19]. Therefore, RANS predictions have to be validated by experimental or DNS data. Second, RANS models do not provide instantaneous flow fields, which have to be considered in many applications such as aircraft noise predictions, swirling flows, etc.

The prohibitive cost of LES, in particular for the investigation of wall-bounded flows at high Reynolds numbers, motivated the development of hybrid RANS-LES methods. In the hybrid RANS-LES modeling approach, a part of the flow domain (the near-wall region) is modeled using RANS methods and the remaining flow domain (away from the wall) is modeled using LES methods. The use of hybrid RANS-LES methods has three main advantages. First, hybrid RANS-LES methods can be used to simulate flows at high Reynolds numbers, which would not be feasible with pure LES [26]. Second, hybrid RANS-LES methods can provide instantaneous flow fields. Third, compared to pure RANS methods, the use of hybrid RANS-LES methods reduces the influence of the choice of the RANS model applied. These advantages make the use of hybrid RANS-LES methods highly attractive for the study of complex engineering and environmental flows at high Reynolds numbers. To illustrate the advantages of using hybrid RANS-LES methods for complex turbulent flow simulations, let us consider the turbulent flow past a sphere. This flow configuration is a representative test case for many external engineering flows. The flow consists of an attached boundary layer, developed upstream of the sphere, and flow separation in the downstream wake region. At low and moderate Reynolds numbers, this flow can be investigated using DNS and LES methods, respectively. However, at high Reynolds numbers either RANS or hybrid RANS-LES methods are required for the numerical simulation. The use of RANS methods has been shown to be inaccurate even for the prediction of the Strouhal number of such flows [27]. However, the use of hybrid methods (RANS in the attached boundary layer and LES in the wake region) led to successful predictions of the Strouhal number and aerodynamic forces on the surface of the sphere, and it provided unsteady flow fields in the downstream wake [28].

Despite their success, there are several problems related to existing hybrid RANS-LES methods. First, there is a large variety of hybrid RANS-LES methods, and most of these methods have been empirically developed (only a few researchers developed hybrid RANS-LES methods on a theoretical basis [21, 29–34]). Hence, there is a need to clarify the most appropriate theoretical basis for developing hybrid RANS-LES methods. Second, most existing hybrid RANS-LES methods do not represent hierarchical (stress transport equation, nonlinear and linear algebraic stress) models, which can be used to address problems of varying complexity. Third, the predictions of most existing hybrid RANS-LES methods have shortcomings, e.g., regarding the mean velocity profile in the log-law region of attached boundary layers [35–38].

The purpose of this paper is to develop computationally the realizable unified RANS-LES models derived by Heinz [33] on the basis of stochastic analysis, and to evaluate the characteristic features of these models. This will be done in terms of *a priori* and *a posteriori* analyses of turbulent channel flow data. The paper is organized in the following way. An overview of existing hybrid RANS-LES methods is given in Sect. 2. Sections 3 and 4 describe the unified RANS-LES modeling and computational approaches, respectively. *A priori* analyses of different coupling approaches are presented in Sect. 5. *A posteriori* analyses of the model properties of unified RANS-LES methods, their accuracy and cost will be presented in Sects. 6, 7, and 8, respectively. The conclusions are summarized in Sect. 9.

2. Existing Hybrid RANS-LES Methods

To prepare the comparison of ways to formulate hybrid RANS-LES methods, let us begin with the consideration of LES and RANS methods. Depending on the model formulation as RANS or LES model, $\widetilde{U}_i$ refers to the mean or filtered velocity. For simplicity, we consider incompressible flow, i.e., $\widetilde{U}_i$ satisfies $\partial \widetilde{U}_k/\partial x_k = 0$. The conservation equation of momentum is given by

$$\frac{\widetilde{D}\widetilde{U}_i}{\widetilde{D}t} + \frac{\partial D_{ik}}{\partial x_k} = -\frac{1}{\rho}\frac{\partial \widetilde{p}}{\partial x_i} + 2\nu \frac{\partial \widetilde{S}_{ik}}{\partial x_k}. \tag{1}$$

Here, $\widetilde{D}/\widetilde{D}t = \partial/\partial t + \widetilde{U}_k \partial/\partial x_k$ denotes the filtered Lagrangian time derivative, and $\widetilde{S}_{ij} = (\partial \widetilde{U}_i/\partial x_j + \partial \widetilde{U}_j/\partial x_i)/2$ is the rate-of-strain tensor. In addition, we have here the filtered pressure $\widetilde{p}$, ρ is the constant mean mass density, and ν is the constant kinematic viscosity. The sum convention is used throughout this paper. Equation (1) is unclosed due to the unknown stress tensor D_{ij}. This stress is usually parametrized as $D_{ij} = kF_{ij}[\widetilde{\boldsymbol{S}}\ L_0/k^{1/2},\ \widetilde{\boldsymbol{\Omega}}\ L_0/k^{1/2}]$. Here, $k = D_{nn}/2$ refers to the turbulent kinetic energy, and F_{ij} is a non-dimensional functional involving in addition to $k^{1/2}$ the rate-of-strain matrix $\widetilde{\boldsymbol{S}}$ with elements $\widetilde{S}_{ij}$, the rate-of-rotation matrix $\widetilde{\boldsymbol{\Omega}}$ with elements $\widetilde{\Omega}_{ij} = (\partial \widetilde{U}_i/\partial x_j - \partial \widetilde{U}_j/\partial x_i)/2$, and a characteristic length scale L_0. Depending on the definition of L_0, Eq. (1) can be used either as a RANS or LES equation. An LES equation is given if L_0 is defined to be proportional to the filter width Δ, which represents an external parameter that has to be provided. A RANS equation is given if L_0 is provided as a characteristic length scale of large-scale turbulence. A difference is often made between RANS and unsteady RANS (URANS) methods, with the understanding that RANS methods provide time-independent solutions, whereas URANS methods provide time-dependent solutions [27]. For simplicity, we will not distinguish between such different types of solutions and only talk about RANS methods. Corresponding to the terminology used for RANS methods, no difference will be made between LES and Very Large Eddy Simulation (VLES) methods.

It turns out that there are many different possibilities to combine RANS and LES methods. Coupled RANS-LES methods are the most commonly used methods. There are two basic ways to couple RANS and LES methods: segregated RANS-LES methods, which use different velocity equations and couple all mean flow and turbulence variables at an interface, and interfaced RANS-LES methods, which use one velocity equation and couple the stress D_{ij} at an interface. The use of segregated methods is described in a variety of applications [27, 39–49]. A general problem is the coupling of RANS and LES variables at the interface. In general, experimental data (which are often unavailable) are required to demonstrate the suitability of RANS results, and an empirical noise model is needed to create instantaneous LES inflow data on the basis of RANS results [47, 50]. Compared to segregated methods, the significant advantage of interfaced methods is the continuous velocity transition between RANS and LES subdomains without discontinuity at the interface [35–38, 51–58]. The most commonly used interfaced approach is the detached eddy simulation (DES) of Spalart et al. [51]. The DES model has been successfully applied to many massively separated flow configurations [35, 51–53]. However, the DES calculation of RANS and LES stresses at the interface implies a jump in the mean velocity profile in the log-law region near the RANS-LES interface (i.e., a spurious buffer layer) of attached flows. Different empirical methods [35, 56, 57] have been proposed to avoid the occurrence of this spurious buffer layer. These empirical methods successfully reduced the size of the spurious buffer layer for the flows investigated, but the applicability of these emprirical approaches to a wide range of flows still has to be investigated. Similar problems regarding the use of other interfaced methods for simulations of attached boundary layers were reported by Breuer et al. [36], Davidson and Peng [37], Hamba [38], Tucker and Davidson [54], Tessicini et al. [55], Kniesner et al. [58].

Another way of combining RANS and LES methods is the use of distributed RANS-LES methods. There are two basic ways of designing such methods: mixed (or blended) RANS-LES methods, which use one velocity equation in conjunction with a combination of RANS and LES stresses at every point, and non-mixed methods, which use one velocity equation in conjunction with either a RANS or LES stress at every point depending on a local criterion that varies smoothly in space. Distributed methods, which have the advantages of being independent of the problems introduced by interfaces, were developed in a variety of alternative ways. Mixed RANS-LES methods were presented, for example, by Speziale [59], Germano [29], and Girimaji [32]. Applications of Speziale's flow simulation methodology can be found in [60–62], applications of Germano's hybrid filtering approach can be found in Sánchez-Rocha and Menon [34], Sagaut and Germano [63], Rajamani and Kim [64], Fadai-Ghotbi et al. [65], Sánchez-Rocha and Menon [66], and applications of Girimaji's Partially Averaged Navier-Stokes (PANS) equations approach can be found in

[67–74] . Non-mixed RANS-LES methods were developed by Heinz on the basis of the mean velocity equation [21] and on the more general basis of stochastic turbulence models [33]. Only preliminary applications of Heinz's model were reported so far [75, 76]. De Langhe et al. [30] used a corresponding formulation of the velocity equation in conjunction with the application of renormalization group theory for the calculation of the subgrid-scale (SGS) viscosity. Applications of the approach of De Langhe et al. [30] were reported by De Langhe et al. [31, 77, 78].

3. A Unified RANS-LES Model

The discussion in the preceding section shows that there is a variety of possibilities to design hybrid RANS-LES methods. Apart from that, many of these methods can be used in several ways, e.g., depending on how the stresses $D_{ij} = kF_{ij}[\widetilde{\boldsymbol{S}}\, L_0/k^{1/2},\ \widetilde{\boldsymbol{\Omega}}\, L_0/k^{1/2}]$ are combined. For example, it is possible to transition from LES to RANS by matching the RANS and LES stresses D_{ij}, or the coefficients $L_0 k^{1/2}$ (turbulent viscosities) of $\widetilde{\boldsymbol{S}}$ and $\widetilde{\boldsymbol{\Omega}}$, or the length scales L_0, or the time scales $L_0/k^{1/2}$. So how is it possible to determine the most appropriate hybrid RANS-LES method?

A basis for addressing this question is given by the general properties of fluid flow equations. The simplest way to see these properties is to consider molecular motion equations [33, 79] that imply the Navier-Stokes equations (see, e.g., equation (2.9b) in reference [33]). These equations are characterized by the following: they represent a realizable fluid flow model that is supported by a proven theory, and the fluid model involves two ingredients: (a) a model for the evolution of velocities in a nondimensional time defined in terms of a characteristic time scale, and (b) a model for the characteristic time scale used to define the nondimensional time. An optimal hybrid RANS-LES model should reflect these fundamental properties of fluid flow equations and have the following properties P1, P2, and P3:

P1: The hybrid RANS-LES model is supported by a proven theory and realizable.

P2: Scale information enters the hybrid model only via the time scale model.

P3: The model for the time scale describes continuous variations between the RANS and LES scale.

Property P1 is relevant to the understanding of the range of applicability of simulation methods. Realizability was proven to represent a valuable guiding principle for turbulence modeling [2, 80–83]. Therefore, an optimal hybrid RANS-LES model should satisfy the property P1. An optimal hybrid RANS-LES model should reflect the relevant property of RANS and LES equations to involve the same velocity model, i.e., the hybrid model should satisfy the property P2. In this way, an optimal hybrid model minimizes the use of modeling assumptions, which are focused on the explanation of time scale variations. The design of a hybrid RANS-LES model then requires that the transition between RANS and LES equations is controlled by a model for the characteristic time scale. An optimal hybrid model will involve a time scale model that describes continuous variations between the RANS and LES scale, which corresponds to property P3. A model that has this property enables simulations without discontinuities or jumps of mean velocity profiles near interfaces. A combination of velocity and time scale models that have the properties

P2 and P3 represents a unified turbulence model because it combines on velocity model with a unified time scale formulation that covers both the RANS and LES scale.

Most hybrid RANS-LES methods described in Sect. 2 do not satisfy all the properties P1, P2, and P3. For example, many hybrid methods are based on *ad hoc* assumptions, which means there is no underlying theory that can explain the structure of equations applied. It is then unclear, for example, in which way such models can be extended to nonlinear stress models. Many methods do also not satisfy the properties P2 and P3 because scale variations are not only covered by variations of one scale-determining time scale, which corresponds to the use of different velocity models in RANS and LES limits. The purpose here is not to provide an analysis of properties of all available hybrid RANS-LES models. Instead, the goal is to show that the unified models derived by Heinz [33] on the basis of stochastic analysis satisfies the properties P1, P2, and P3, and to further investgate the suitability of these models.

3.1. A Unified RANS-LES Model

Heinz's unified model [33] was developed as a model for the evolution of the probability density function (PDF) of turbulent velocities. Incompressible flow is considered again (the compressible formulation can be found elsewhere [33]). The unified model enables the derivation of transport equations for all the moments of the PDF. The model does exactly reproduce the incompressibility constraint $\partial \widetilde{U}_k / \partial x_k = 0$ and the conservation of momentum equation (1). For the stress tensor, which appears as an unknown in the momentum equation, the PDF model implies the equation

$$\frac{\widetilde{D} D_{ij}}{\widetilde{D} t} + \frac{\partial T_{kij}}{\partial x_k} = -D_{ik} \frac{\partial \widetilde{U}_j}{\partial x_k} - D_{jk} \frac{\partial \widetilde{U}_i}{\partial x_k} - \frac{2}{\tau_L} \left(D_{ij} - \frac{c_o}{3} D_{kk} \delta_{ij} \right). \tag{2}$$

Here, T_{ijk} is the triple correlation tensor of velocity fluctuations, τ_L is the Lagrangian relaxation time scale of turbulent velocity fluctuations, and c_o is a model constant. For the following discussion it is helpful to rewrite Eq. (2) for D_{ij} in terms of equations for the turbulent kinetic energy $k = D_{nn}/2$ and standardized anisotropy tensor $d_{ij} = (D_{ij} - 2k\delta_{ij}/3)/(2k)$. These equations are given by [33]

$$\frac{\widetilde{D} k}{\widetilde{D} t} + \frac{1}{2} \frac{\partial T_{knn}}{\partial x_k} + 2k d_{kn} \frac{\partial \widetilde{U}_n}{\partial x_k} = -\frac{2(1 - c_o)k}{\tau_L}, \tag{3}$$

$$\frac{\widetilde{D} d_{ij}}{\widetilde{D} t} + \frac{1}{2k} \frac{\partial (T_{kij} - T_{knn}\delta_{ij}/3)}{\partial x_k} + \frac{d_{ij}}{k} \frac{\widetilde{D} k}{\widetilde{D} t} + d_{ik} \frac{\partial \widetilde{U}_i}{\partial x_k} - \frac{2}{3} d_{kn} \frac{\partial \widetilde{U}_n}{\partial x_k} \delta_{ij} = -\frac{2}{\tau_L} d_{ij} - \frac{2}{3} \widetilde{S}_{ij}. \tag{4}$$

These equations can be used to derive a consistent hierarchy of deterministic models, which is helpful for working with models that are chosen according to the complexity of the flow considered. One option of using Eqs. (1), (3), and (4) is to close these equations by a model for the triple correlation T_{ijk}, which is implied by the PDF transport equation considered [21, 84]. A second option is to reduce the computational effort significantly by using Eq. (4) for the development of an algebraic model for the stress D_{ij}. A first-order approximation for D_{ij} can be obtained by neglecting the left-hand side terms in Eq. (4), which results in $d_{ij} = -\widetilde{S}_{ij} \tau_L / 3$. The latter expression implies that D_{ij} is found in the first order of approximation as

$$D_{ij} = \frac{2}{3} k \delta_{ij} - 2\nu_t \widetilde{S}_{ij}, \tag{5}$$

where the turbulent viscosity ν_t is given by $\nu_t = k\tau_L/3$. A second-order approximation for D_{ij} can be obtained by neglecting the transport terms (the first three terms) and using the first-order approximation $d_{ij} = -\widetilde{S}_{ij}\tau_L/3$ to replace d_{ij} in the production terms on the left-hand side of Eq. (4) [33]. However, such a quadratic stress model will be not considered here because the focus of this paper is on the analysis of fundamental properties of unified RANS-LES models.

The model obtained satisfies the properties P1, P2, and P3 of an optimal hybrid RANS-LES model. The model satisfies the property P1. The stress model is implied by the underlying stochastic turbulence model, which is well supported [33]. Realizability is guaranteed in the sense that these equations are derived as a consequence of a realizable stochastic turbulence model. A further discussion of the realizability problem is given in Sect. 6.1. Property P2 is also satisfied: RANS and LES equations have the same structure. The only difference is given by the specification of the time scale τ_L applied. Property P3 can be satisfied by defining the time scale in the following way Heinz [33],

$$\tau_L = min(\tau_L^{LES}, \tau_L^{RANS}). \tag{6}$$

Here, τ_L^{LES} and τ_L^{RANS} represent typical time scales used in LES and RANS approaches. According to this definition, Eq. (1) combined with Eq. (2) (or Eq. (5)) represents a usual LES or RANS equation depending on whether τ_L^{LES} is smaller than τ_L^{RANS} or not, respectively. The model (6) represents the simplest possible model for τ_L. The validity of this assumption will be shown in Sect. 5.2. It is worth noting that this unification approach is more general than the unification of mean velocity equations [21, 30]: by focusing the unification of methods on the scale-determining variable τ_L, the unification provides a hierarchy of deterministic models.

3.2. RANS-LES Coupling Approaches

The use of the time scale relation $\tau_L = min(\tau_L^{LES}, \tau_L^{RANS})$ requires the definition of τ_L^{LES} and τ_L^{RANS}. Eqs. (1) and (2) represent pure LES equations if the time scale τ_L is a linear function of the filter width Δ,

$$\tau_L^{LES} = \ell_* \tau^{LES}, \tag{7}$$

where $\ell_* = (1 \pm 0.5)/3$ and $\tau^{LES} = \Delta/k^{1/2}$, see [21]. On the other hand, Eqs. (1) and (2) represent pure RANS equations if τ_L is given by

$$\tau_L^{RANS} = 2(1 - c_o)\tau^{RANS}, \tag{8}$$

where τ^{RANS} represents the dissipation time scale of turbulence. The validity of the latter relation can be seen by using Eq. (8) in Eq. (3), which shows that the last term in Eq. (3) represents the negative dissipation rate. The model parameter c_o varies slightly depending on whether Eqs. (1) and (2) are used as LES or RANS equations. For the LES regime we have $c_o = 19/27 \approx 0.7$, and for the RANS regime we have $c_o = 0.83 \pm 0.7$, see Heinz [33]. The simulation results reported below show that the influence of such minor c_o variations is negligible. In conjunction with a theoretical reasoning [33], it is, therefore, well justified to set $\ell_* = 2(1 - c_o)$. The use of the standard value

$\ell_* = 1/3$ would imply $c_o = 5/6 \approx 0.83$, which corresponds to the standard RANS value of c_o. Hence, τ_L^{RANS} can be written

$$\tau_L^{RANS} = \ell_* \tau^{RANS}. \tag{9}$$

The application of this relation requires the definition of τ^{RANS}. This question can be conveniently addressed by considering an equation for the turbulence frequence ω, which determines τ^{RANS} via the definition $\tau^{RANS} = 1/\omega$. The usual structure of the ω equation is given by

$$\frac{\widetilde{D}\omega}{\widetilde{D}t} = F\left[S^2, k, \omega, \nu, \nu_t\right], \tag{10}$$

see, for example, Eq. (16). Here, F refers to a functional of $S^2 = 2\widetilde{S}_{nk}\widetilde{S}_{nk}$, k, ω, ν, and ν_t, and the gradients of these variables in space. The turbulent viscosity $\nu_t = k\tau_L/3$ in Eq. (10) involves the time scale τ_L, which switches between the LES and RANS regimes. Instead of using Eq. (10) it would be possible to replace ν_t in (10) by the RANS limit ν_t^{RANS} in order to ensure that the ω equation provides the RANS time scale $\tau^{RANS} = 1/\omega$. However, there is no difference between this option and Eq. (10): ω is used in the unified approach only if $\tau_L = \tau_L^{RANS}$, and in that case we apply $\nu_t = \nu_t^{RANS}$ in Eq. (10).

According to Eq. (6) combined with (7) and (9), the unified time scale τ_L is given by

$$\tau_L = \ell_* min(\Delta k^{-1/2}, \tau^{RANS}) = \ell_* min(\Delta, L) k^{-1/2}, \tag{11}$$

where the characteristic length scale $L = k^{1/2}\tau^{RANS}$ of turbulence is introduced. It is relevant to note that L is not equal to the characteristic RANS length scale of large scale turbulence because the turbulent kinetic energy k is provided through the unified RANS-LES simulation. Relation (11) can be used in several ways that correspond to different coupling methods of RANS and LES equations. These coupling options will be discussed in the following three paragraphs and validated in Sect. 5.

A first approach, the exact coupling (EC) approach, is given by providing τ^{RANS} in $\tau_L = \ell_* min(\Delta k^{-1/2}, \tau^{RANS})$ by a pure RANS approach as described above. The RANS simulation is performed prior to the unified RANS-LES simulation so that the dissipation time scale τ^{RANS} is unaffected by LES. The turbulent kinetic energy k in $\tau_L = \ell_* min(\Delta k^{-1/2}, \tau^{RANS})$ is provided through the unified RANS-LES simulation. This coupling approach corresponds to the idea of providing the strict RANS limit for τ_L. Its disadvantage is the need to do a RANS simulation in addition to the unified RANS-LES simulation and to store the resulting τ^{RANS} data.

A second approach, the dynamic coupling (DC) approach, is given by providing τ^{RANS} and k in the relation $\tau_L = \ell_* min(\Delta k^{-1/2}, \tau^{RANS})$ by the unified RANS-LES simulation, which means τ^{RANS} is provided via Eq. (10) which obtains the required input from the unified RANS-LES simulation. This coupling approach corresponds to the idea of calculating the transition between RANS and LES regions dynamically as part of the unified RANS-LES simulation. This option is very attractive because it avoids the need for a separate RANS simulation, and it provides results that are (compared to the EC coupling approach) less affected by shortcomings of the RANS method applied (which are often not fully known). Thus, this option is well appropriate to study complex flows for which RANS models have not been validated or are known to fail. This coupling method has been successfully applied on the basis of the model of De Langhe et al. [31] to the prediction of turbulent swirling flows.

A third approach, the fixed coupling (FC) approach, is given by providing L in $\tau_L = \ell_* min(\Delta, L)/k^{1/2}$ by a pure RANS approach prior to the unified RANS-LES simulation, whereas the denominator $k^{1/2}$ is obtained via the unified RANS-LES method. This approach recovers the correct LES limit $\tau_L^{LES} = \Delta k^{-1/2}$ of τ_L, and it provides a RANS limit $\tau_L^{RANS} = \ell_* L/k^{1/2}$. The latter limit approximates the exact RANS limit by the assumption that $k^{1/2}$ provided by the unified model in the RANS region corresponds to $k^{1/2}$ provided by the pure RANS method. This coupling approach corresponds to the idea of fixing the transition between RANS and LES regions prior to the simulation, which may be helpful for certain flows [26]. The disadvantage of this option is the need to do a RANS simulation in addition to the unified RANS-LES simulation and to store the resulting data.

3.3. Linear Unified RANS-LES Model

Next, the model applied in the following will be fully specified. The model described in this subsection will be referred to as linear unified model (LUM). The flow is described by the incompressibility condition $\partial \widetilde{U}_k/\partial x_k = 0$ and the velocity equation

$$\frac{\widetilde{D}\widetilde{U}_i}{\widetilde{D}t} = -\frac{\partial(\langle p \rangle/\rho + 2k/3)}{\partial x_i} + 2\frac{\partial(\nu+\nu_t)\widetilde{S}_{ik}}{\partial x_k}. \tag{12}$$

The turbulent viscosity is given by $\nu_t = k\tau_L/3$, and the turbulent kinetic energy equation reads according Eq. (3)

$$\frac{\widetilde{D}k}{\widetilde{D}t} = -\frac{1}{2}\frac{\partial T_{knn}}{\partial x_k} + 2\frac{k\tau_L}{3}\widetilde{S}_{nk}\frac{\partial \widetilde{U}_n}{\partial x_k} - \frac{2(1-c_o)k}{\tau_L} = -\frac{1}{2}\frac{\partial T_{knn}}{\partial x_k} + 2\nu_t\widetilde{S}_{nk}\widetilde{S}_{nk} - \frac{2(1-c_o)k}{\tau_L}, \tag{13}$$

where $d_{ij} = -\widetilde{S}_{ij}\tau_L/3$, $\nu_t = k\tau_L/3$, and the definition of $\widetilde{S}_{nk}$ are used. This equation requires a model for the triple correlation. Such a model is given by

$$T_{knn} = -2(\nu+\nu_t)\frac{\partial k}{\partial x_k}. \tag{14}$$

The structure of this expression can be derived as a consequence of the transport equation for triple correlations, which is implied by the PDF transport equation considered [21]. This expression is extended here by the consideration of the kinematic viscosity ν. By using $S^2 = 2\widetilde{S}_{nk}\widetilde{S}_{nk}$ we can write the turbulent kinetic energy equation as

$$\frac{\widetilde{D}k}{\widetilde{D}t} = \frac{\partial}{\partial x_k}\left[(\nu+\nu_t)\frac{\partial k}{\partial x_k}\right] + \nu_t S^2 - \frac{2(1-c_o)k}{\tau_L}. \tag{15}$$

The calculation of the time scale τ_L requires the calculation of $\tau^{RANS} = 1/\omega$. To determine ω we specify the general ω equation (10) by using the model of Bredberg et al. [85],

$$\frac{\tilde{D}\omega}{\tilde{D}t} = C_{\omega 1}\frac{\omega}{k}\nu_t S^2 - \frac{C_{\omega 2}}{C_k}\omega^2 + \frac{\partial}{\partial x_j}\left[(\nu + \frac{\nu_t}{\sigma_\omega})\frac{\partial \omega}{\partial x_j}\right] + \frac{C_\omega}{k}(\nu+\nu_t)\frac{\partial k}{\partial x_j}\frac{\partial \omega}{\partial x_j}. \tag{16}$$

Here, $C_{\omega 1}$, $C_{\omega 2}$, C_ω, and σ_ω are model constants that have the values

$$C_{\omega 1} = 0.49, \qquad C_{\omega 2} = 0.072, \qquad C_k = 0.09 \qquad C_\omega = 1.1, \qquad \sigma_\omega = 1.8. \tag{17}$$

The comparison with the RANS limit $\nu_t^{RANS} = \ell_* k \tau^{RANS}/3$ of ν_t used in Eqs. (15) and (16) with the RANS viscosity $\nu_t^{RANS} = C_k k/\omega$ used in the model of Bredberg et al. [85] reveals the consistency constraint

$$\ell_* = 3C_k. \tag{18}$$

Hence, the use of $C_k = 0.09$ corresponds to $\ell_* = 0.27$, which is close to the standard value $\ell_* = 1/3$ for ℓ_*, see [21]. When the ω equation is integrated through the viscous sublayer ($y^+ \leq 5$), numerical errors can distort the velocity profiles in the viscous sublayer and the log layer [19]. To avoid this problem, the value of ω at the first grid point is set explicitly using the following expression [86]

$$\omega = \sqrt{\left(\frac{2\nu}{y^2}\right)^2 + \left(\frac{C_k^{0.75} k^{0.5}}{\kappa y}\right)^2}, \tag{19}$$

where $\kappa = 0.41$. The resulting expression for ω^2 represents a combination of two terms which are used in conjunction with models that integrate to the wall (first-term) and that apply a wall function (second-term). Correspondingly, the use of Eq. (19) allows the first grid point to be located in the viscous sublayer, in the buffer layer, or in the log law region.

The turbulent viscosity $\nu_t = k\tau_L/3$ derived above does not account for the damping effect of walls on turbulent quantities. This effect can be taken into account by using a modified turbulent viscosity ν_{t*} defined by

$$\nu_{t*} = f_\mu \nu_t. \tag{20}$$

The damping function f_μ used in this relation is defined by

$$f_\mu = 0.09 + \left(0.91 + \frac{1}{Re_t^3}\right)\left(1 - e^{-(Re_t/25)^{2.75}}\right). \tag{21}$$

The turbulence Reynolds number is given here by $Re_t = \nu_t/\nu$. The turbulent viscosity ν_t in Eqs. (20)-(21) refers to the use of the RANS viscosity $\nu_t^{RANS} = \ell_* k \tau^{RANS}/3$ or LES viscosity $\nu_t^{LES} = \ell_* k \tau^{LES}/3$ depending on whether τ^{RANS} or τ^{LES} is used. The RANS mode of the damping function (21) ensures the correct scaling $O(y^3)$ of the turbulent viscosity in the near-wall region: by using a Taylor series expansion [19, 85] we find $\nu_t^{RANS} \sim O(y^4)$ and $f_\mu^{RANS} \sim O(1/y)$. The damping function (21) was suggested by Bredberg et al. [85] to improve the agreement between RANS simulations and channel flow DNS. This damping function model has been tested by several benchmark and complex flow simulations [87]. The use of Eq. (21) in the LES mode, which is suggested here, is a natural choice for the unified RANS-LES modeling approach. The reason for this choice is that it provides a smooth variation of the damping function through the RANS-LES interface if the interface is located relatively close to the wall such that the damping function affects both, RANS and LES regions. The suitability of using Eq. (21) in the LES mode was proven by simulations in which Eq. (21) was only applied in the RANS region (i.e., $f_{\mu} = 1$ in the LES region). Such simulations (not shown) revealed significant shortcomings compared to simulations in which Eq. (21) was used for both RANS and LES regions.

4. Numerical Method

A sketch of the computational domain is shown in Fig. 1. The domain size ($L_x * L_y * L_z$) depends on the friction Reynolds number $Re_\tau = u_\tau \delta/\nu$. Here, $u_\tau = \sqrt{\tau_w/\rho}$ is the friction velocity, τ_w is the wall shear stress, δ is the half channel width, and ν is the kinematic viscosity. The unified simulations were performed using the same code, whereas the DNS simulations were performed using a different code.

DNS calculations have been performed using an incompressible Navier-Stokes solver [88, 89]. The algorithm employs spectral discretization (Fourier modes along the periodic directions and Chebyshev polynomials along the wall normal direction) for the spatial derivatives. The convection term was formulated in the skew-symmetric form to avoid aliasing errors. It has been computed explicitly. The viscous term was treated implicitly. Time marching was performed using a fourth-order backward difference scheme. The pressure gradient that drives the flow in the channel has been adjusted dynamically to maintain a constant mass flow rate. Periodic boundary conditions were employed along the streamwise (x) and spanwise (z) direction while a no slip boundary condition has been employed along the wall normal direction (y). The time step was modified dynamically to ensure a constant CFL number of 0.5. The total time of simulation was $t = 320\,\delta/u_\tau$. A time period of approximately $t = 100\,\delta/u_\tau$ was used for the calculation of the flow development. The statistics were then taken over a time period $t = 220\,\delta/u_\tau$. The DNS computations were performed using the spectral code for $Re_\tau = 395$ corresponding to a Reynolds number $Re = U_b L_y/\nu = 13350$, where U_b refers to the bulk velocity. The domain size was $2\pi * 2 * \pi$, and the grid applied was $256 * 193 * 192$ [90]. The results of these DNS were proven to agree very well with the corresponding DNS results of Moser et al. [90],

The unified RANS-LES models have been implemented in the OpenFOAM CFD Toolbox [86]. The calculations have been performed using a finite-volume based method with the numerical grid being used as the LES filter. The convection term was discretized using a second-order central difference scheme in the momentum equation and a bounded second-order central difference scheme in the turbulence transport equations to ensure a stable solution. All other terms were discretized using a second-order central difference scheme. The pressure gradient that drives the flow in the channel has been adjusted dynamically to maintain a constant mass flow rate. PISO algorithm was used for the pressure-velocity coupling [91]. The resulting algebraic equations for all the flow variables except the pressure have been solved iteratively using a preconditioned biconjugate gradient method with a diagonally incomplete LU preconditioning at each time step. The Poisson equation for the pressure was solved using an algebraic multigrid (AMG) solver. When the scaled residual became less than 10^{-6}, the algebraic equations were considered to be converged. Time marching was performed using a second-order backward difference scheme. The time step was modified dynamically to ensure a constant CFL number of 0.5. Periodic boundary conditions have been employed along the streamwise and spanwise directions for all the flow variables. Along the wall normal direction, a no slip boundary condition was used for velocity and the modeled turbulent kinetic energy was set to zero. For ω, Eq. (19) was used at the first near-wall grid point as the boundary condition. Unified RANS-LES simulations have been performed at a variety of friction Reynolds numbers Re_τ with domain sizes specified in Table 1. Details about the grids applied (including the normalized $\Delta x^+, \Delta z^+, \Delta y^+$ values) are given in Table 2. A simulation time $t = 100\,\delta/u_\tau$ was used to eliminate the effect of the initial conditions. Statistics were then taken over at least $t = 220\,\delta/u_\tau$.

The results reported in the following sections require the calculation of different ensemble averaged and filtered variables. The calculation of these variables from DNS data is explained here. The ensemble mean $\langle F \rangle_e$ of any variable F is calculated by

$$\langle F \rangle_e = \frac{1}{N_t N_x N_z} \sum_{i=1}^{N_t} \sum_{j=1}^{N_x} \sum_{k=1}^{N_z} F_{ijk}(x, y, z, t). \tag{22}$$

Here, N_t is the number of temporal samples used for the averaging, and N_x and N_z are the number of points in the streamwise and spanwise directions, respectively. For $N_t = 1$, the ensemble averaging involved a sample size of $256 * 192 = 49,152$ taken in x and z directions at every wall-normal location considered in the *a priori* analysis. For this sample size, the statistical error of predictions is below 0.9% [84]. Hence, all the analyses were performed by setting $N_t = 1$. The ensemble mean of the instantaneous velocity field was calculated using Eq. (22). The ensemble means of the turbulent kinetic energy and dissipation rate were calculated from the ensemble mean of the velocity and its gradients using the expressions

$$k^{RANS} = 0.5 \left[\langle U_i U_i \rangle_e - \langle U_i \rangle_e \langle U_i \rangle_e \right], \qquad \epsilon^{RANS} = 2\nu \left[\langle S_{ij} S_{ij} \rangle_e - \langle S_{ij} \rangle_e \langle S_{ij} \rangle_e \right]. \tag{23}$$

Assuming a box filter, the filtered value $\widetilde{F}$ of any variable F is calculated by

$$\widetilde{F}(x, y, z, t) = \frac{1}{\Delta_x \Delta_z} \int_{x-\Delta_x/2}^{x+\Delta_x/2} \int_{z-\Delta_z/2}^{z+\Delta_z/2} F(x, y, z, t) dx dy dz. \tag{24}$$

The trapezoidal rule is used for the integration. The integration is not performed along the wall-normal direction because of the non-uniformity of the grid (filtering and differentiation operators do not commute and this introduces numerical errors [2]). This approach of filtering only in the homogenous directions is usually applied for performing *a priori* studies [5–7, 92–94]. The magnitude of the streamwise and spanwise spacing Δ_x and Δ_z was varied in the following way: $\Delta_x^{DNS} \leq \Delta_x \leq 20\Delta_x^{DNS}$ and $\Delta_z^{DNS} \leq \Delta_z \leq 20\Delta_z^{DNS}$, respectively. The filtered velocity field was calculated using Eq. (24). The kinetic energy and dissipation rate are calculated from the filtered instantaneous velocity field $\widetilde{U}$ and its gradient as follows,

$$k = 0.5(\widetilde{U_i U_i} - \widetilde{U_i}\widetilde{U_i}), \qquad \epsilon = 2\nu(\widetilde{S_{ij} S_{ij}} - \widetilde{S_{ij}}\widetilde{S_{ij}}). \tag{25}$$

It is worth noting that k and ϵ obtained in this way represent unified variables: depending on the filter width applied they range from LES variables to RANS variables. All the results shown below have been averaged along the homogeneous directions.

5. *A Priori* Analysis of Coupling Approaches

The unification of RANS and LES equations was achieved in Sect. 3.2 by defining the unified time scale as $\tau_L = \ell_* min(\tau^{LES}, \tau^{RANS})$. This assumption leads to three relevant questions. The first question is how the filter width Δ in $\tau^{LES} = \Delta / k^{1/2}$ should be defined. According to $\tau_L = \ell_* min(\tau^{LES}, \tau^{RANS})$, the filter width Δ determines the location of the RANS-LES interface, which has a significant effect on the predictions of the unified model. The second question is about the suitability of switching between RANS and LES according to the definition $\tau_L = \ell_* min(\tau^{LES}, \tau^{RANS})$. The latter choice is the simplest possible assumption, and the question is whether other ways for performing the transition between RANS and LES are more appropriate. The third question is about the most appropriate way to provide τ^{RANS}, which is the question about the most appropriate coupling approach. This question definitely has an influence on the computational efficiency, see the discussion of coupling approaches and their computational consequences in Sect. 3.2. These three questions will be addressed in the following three subsections, respectively. The instantaneous data required for this analysis were taken from the DNS performed for the $Re_\tau = 395$ case. Such simulations are computationally efficient and sufficient for significantly reducing the influence of Reynolds number effects.

5.1. Choice of Filter Width

A variety of definitions of the filter width have been used for hybrid RANS-LES simulations on structured grids: the geometric mean of a cell, $\Delta = (\Delta_x \Delta_y \Delta_z)^{1/3}$ [2], the smallest side of a cell, $\Delta = \min(\Delta_x, \Delta_y, \Delta_z)$ [37], the maximum area of cell faces, $\Delta = (\max(\Delta_x\Delta_y, \Delta_x\Delta_z, \Delta_y\Delta_z))^{1/2}$ [95], and the large side of a cell, $\Delta = \max(\Delta_x, \Delta_y, \Delta_z)$ [52]. An advantage of the geometric mean and face area filter width is that these filters can be used in a straightforward way on unstructured and hybrid grids. To account for the grid anisotropy, these filter width definitions were considered by multiplying the filter width definition with the anisotropy function [96]

$$f(a_1, a_2) = \cosh \sqrt{4\left[(\ln(a_1) - \ln(a_2))^2 + \ln(a_1)\ln(a_2)\right]/27}. \tag{26}$$

We use here $a_1 = \Delta_1 / \max(\Delta_x, \Delta_y, \Delta_z)$ and $a_2 = \Delta_2 / \max(\Delta_x, \Delta_y, \Delta_z)$, where Δ_1 and Δ_2 represent the two cell sides that are smaller than $\max(\Delta_x, \Delta_y, \Delta_z)$. The variation of the filter width according to these four choices was calculated by using the DNS-RANS grid. The results are shown along the wall-normal direction (the grid spacing is constant along the streamwise and spanwise directions) in Fig. 2. This figure shows that there are significant differences between the filter width definitions. The small side filter gives the minimum value for the filter width, and the large side filter gives the maximum value. The face area filter width is slightly smaller than the large side filter width, while the geometric mean width has almost the half of the value of the large side filter width. Such differences will vary with the grid refinement or coarsening. However, the small side filter width will be not affected because $\Delta_y \ll (\Delta_x, \Delta_z)$ in wall-bounded flow simulations.

The suitability of different filter width definitions can be studied by considering the corresponding implications for the LES-RANS transition. By coarsening the grid, the unified method will switch from LES to RANS if the grid becomes very coarse. For such a very coarse grid, the unified time scale $\tau_L = min(\tau_L^{LES}, \tau_L^{RANS})$ has to provide τ_L^{RANS} for all definitions of Δ, which requires that $\tau_{LES} > \tau_{RANS}$ everywhere in the domain. The LES time scale is always given by $\tau^{LES} = \Delta k^{-1/2}$. We combine the investigation of this question with the consideration of the suitability of the three coupling approaches discussed in Sect. 3.2, this means the RANS time scale will be defined as

$$\tau_{EC}^{RANS} = \frac{k^{RANS}}{\epsilon^{RANS}}, \qquad \tau_{DC}^{RANS} = \frac{k}{\epsilon}, \qquad \tau_{FC}^{RANS} = \frac{k^{RANS}}{\epsilon^{RANS}} \sqrt{\frac{k^{RANS}}{k}}. \tag{27}$$

The corresponding values of k and ϵ are defined by the relations (23) and (25). It is worth emphazising that the choice of the coupling approach may have a significant effect on the definition of τ_{RANS}. The latter fact is shown in Fig. 3, which shows $\tau_{DC}^{RANS}/\tau_{EC}^{RANS}$ and $\tau_{FC}^{RANS}/\tau_{EC}^{RANS}$ for four different grids. This figure does also show that both τ_{DC}^{RANS} and τ_{FC}^{RANS} converge to τ_{EC}^{RANS} with increasing grid coarsening, as required by the definition of these time scales.

The question of whether all filter width definitions satisfy the requirement described in the preceding paragraph will be considered by using the DNS - RANS grid for which $\Delta_x = 20\Delta_x^{DNS}$, $\Delta_y = \Delta_y^{DNS}$, and $\Delta_z = 20\Delta_z^{DNS}$. This grid is very coarse along the streamwise and spanwise directions. As may be seen in Fig. 3, τ_{DC}^{RANS} and τ_{FC}^{RANS} are very close to τ_{EC}^{RANS}. Thus, for this grid, the unified model should provide the RANS limit everywhere in the domain. The plots of LES and RANS time scales (given in seconds) for the EC, DC and FC approaches are shown in Figs. 4a-d for the small side, geometric mean, face area and large side filter width definitions, respectively. These results show that the small side and geometric filter width definitions are inappropriate because they cause the LES time scale to be smaller than the RANS time scale. Their use would imply LES regions in the flow field on this very coarse grid, which results in erroneous predictions because LES calculations become inaccurate on coarse grids. Regarding the large side filter, the requirement $\tau_{LES} > \tau_{RANS}$ is satisfied by all the coupling approaches, but for the face area filter, $\tau_{LES} > \tau_{RANS}$ is not satisfied for the FC approach. Consequently, the large side filter will be applied in the following. This approach is also well appropriate for comparisons with other hybrid RANS-LES methods like DES, which usually apply the large side filter [26].

5.2. *Choice of Transfer Function*

In Sect. 3.2 we introduced the model $\tau_L = \ell_* min(R_\tau, 1)\tau^{RANS}$ for the unified time scale, where we introduced the time scale ratio $R_\tau = \tau^{LES}/\tau^{RANS}$. Here, $\tau^{LES} = \Delta k^{-1/2}$, and the definition of τ^{RANS} depends on the coupling approach applied (see Sect. 3.2). The model $\tau_L = \ell_* min(R_\tau, 1)\tau^{RANS}$ is the simplest possible choice, so let us have a closer look at its suitability. For doing this we rewrite the time scale model in the following way. The last term in Eq. (13) shows that the unified dissipation rate is given by $\epsilon = \ell_* k/\tau_L$, where $\ell_* = 2(1 - c_o)$ is used. Hence, the unified Lagrangian time scale is given by $\tau_L = \ell_* \tau$, where $\tau = k/\epsilon$ represents the unified dissipation time scale. Correspondingly, the unified time scale model $\tau_L = \ell_* min(R_\tau, 1)\tau^{RANS}$ implies that $\tau = min(R_\tau, 1)\tau^{RANS}$. By introducing the transfer function $T(R_\tau) = \tau/\tau^{RANS}$, the claim made in Sect. 3.2 is that we can use the model $T(R_\tau) = min(R_\tau, 1)$ for the transfer function.

The claim $T(R_\tau) = min(R_\tau, 1)$ can be proven by comparing $T(R_\tau)$ models with DNS calculations of $T(R_\tau)$. Due to its definition $T(R_\tau) = \tau/\tau^{RANS}$, the transfer function can be calculated from DNS data by the expression

$$T(R_\tau) = \frac{k/\epsilon}{k_{RANS}/\epsilon_{RANS}}. \tag{28}$$

The values of k_{RANS} and ϵ_{RANS} follow from the relations (23), and the values of k and ϵ follow from the relations (25). A reasonable model for the transfer function $T(R_\tau)$ is given by [33]

$$T(R_\tau) = \frac{1}{2}R_\tau - \frac{\lambda}{2}\ln\left[\frac{\cosh((1-R_\tau)/\lambda)}{\cosh(1/\lambda)}\right]. \tag{29}$$

In difference to the expression $T(R_\tau) = min(R_\tau, 1)$ used before, this model provides a smooth transition between R_τ and one. For λ = 0, we find that $T(R_\tau) = min(R_\tau, 1)$. The suitability of this model and the optimal setting of the smoothing parameter λ will be considered in the following regarding the EC, DC, and FC coupling approaches. Hence, the model function (29) will be considered in dependence on $R_\tau = \tau^{LES}/\tau^{RANS}_{EC}$, $R_\tau = \tau^{LES}/\tau^{RANS}_{DC}$, and $R_\tau = \tau^{LES}/\tau^{RANS}_{FC}$ for the EC, DC, and FC coupling approaches, respectively. Here, the RANS time scales involved are calculated according to the relations (27).

The comparison between the exact transfer function (28) and model transfer function (29) is shown in the Figs. 5, 6, and 7 for the EC, DC, and FC approach, respectively. The model transfer function (29) is plotted for three different λ values ($0,\ 0.25,$ and 0.5). It can be seen that the model tranfer function of all three coupling approaches provides for the different values of λ a good model for the exact transfer function. To determine an optimal value of λ, the error between the exact and model transfer functions is shown in Figs. 5, 6, and 7 regarding the DNS-C grid, which is typically used for channel flow simulation with hybrid RANS-LES methods. The error was calculated as

$$E_\lambda = 100\sqrt{\sum_{i=1}^{N}(T_i^E - T_i^M)^2}\Big/\sqrt{\sum_{i=1}^{N}(T_i^E)^2}, \tag{30}$$

where T_i^E and T_i^M refer to the exact and model transfer function values, respectively, at the grid point considered. For the EC, DC, and FC coupling approaches the error was found to be minimal for $\lambda = (0.23, 0.2, 0.2)$, respectively. The differences between the use of the latter λ values and the use of $\lambda = 0$ were found to be negligible in simulations: the effects on the mean velocity and stresses were below 0.02%. Thus, all further simulations have been performed for $\lambda = 0$.

5.3. *Choice of Coupling Approach*

The third question addressed in this section concerns the suitability of coupling approaches. Fig. 8 shows the RANS time scales for the three coupling approaches considered on four different grids: DNS - F, DNS - R, DNS - C and DNS - RANS. The corresponding LES time scales are also shown for a comparison. It may be seen that τ^{RANS}_{EC} is unaffected by the grid applied, as required by the definition of this time scale. Regarding τ^{RANS}_{DC} we observe minor variations with the grid, whereas τ_{FC}^{RANS} is strongly affected by the grid. This fact indicates that the use of the FC coupling approach is less appropriate than the use of the EC and DC coupling approaches.

Further insight into this question can be obtained by considering the transfer function $T(R_{\tau}) = min(R_{\tau}, 1)$ for the three coupling approaches on the grids considered in Fig. 8. The corresponding plots are presented in Fig. 9. The value of the transfer function shows in which flow regions RANS and LES are applied: RANS simulations are performed if $T = 1$, and LES is performed for $T < 1$. It may be seen that (outside the viscous region) there is no difference between the coupling approaches for the DNS - F and DNS - RANS grids: all coupling approaches correspond to LES and RANS simulations, respectively. Differences between the coupling approaches may be seen for the DNS - R and DNS - C grids, for which all coupling approaches involve both RANS and LES regions. As required, the RANS region becomes more extended with a growing grid coarsening. A relevant conclusion is that the DC approach provides the largest RANS region among the coupling approaches. This is a desired feature because previous studies with hybrid RANS-LES models showed that the simulation results improve with a growing distance of the RANS - LES interface from the wall [55]. Correspondingly, the DC coupling approach will be used below.

6. *A Posteriori* Analysis of Model Properties

In the last paragraph of Sect. 3.1 it was argued that the unified RANS-LES model presented here satisfies the properties P1, P2, and P3 of an optimal hybrid RANS-LES model, which were formulated in the beginning of Sect. 3. Some specific questions related to these model properties will be addressed in the following. These analyses were performed by applying the LUM in simulations at $Re_{\tau} = 395$.

6.1. Realizability

The conclusion obtained in Sect. 3 that the LUM satisfies the realizability constraint is a consequence of the fact that the RANS-LES equations were derived as a consequence of a realizable stochastic turbulence model. However, there is also another notion of realizability focusing directly on the properties of the stress tensor. This realizability condition requires that the stress tensor is non-negative definite, as required by its definition. According to Schumann [82], the Reynolds stress tensor satisfies this condition if the three principal invariants $I_1 = D_{ii}$, $I_2 = D_{ii}D_{jj} - (D_{ij})^2$ and $I_3 = det(D_{ij})$ of the stress tensor have non-negative values. Vreman et al. [80] considered the same question regarding the SGS stress tensor. They showed that the SGS stress tensor has to satisfy the same realizability conditions as the Reynolds stress tensor. In addition, the non-negativeness of the spatial filter function, $G(\vec{r}) \geq 0$, for all $\vec{r}$ was found to be required to ensure the realizability of SGS stress tensor. It is worth noting that the derivation of turbulence models from an underlying stochastic model in general cannot ensure that the stress tensor is non-negative definite. Apart from that, the use of empirical damping functions in the near-wall region and numerical errors in simulations may imply that the model is non-realizable [97].

The realizability of the LUM was investigated over a wide range of grid sizes by calculating the three principal invariants I_1, I_2, and I_3 of the unified stress tensor. The calculation followed the analysis of Fureby and Tabor [97].

For each simulation, ten time steps were selected at instants well separated in time (the time interval was $100\,\delta/u_\tau$) so that they can be considered to be statistically independent. The principal invariants I_1, I_2, and I_3 were calculated as averages over these times. The number of grid points and the percentage of grid points at which the realizability conditions were violated are shown in Table 3 for the different grids considered. Realizability constraint violations were observed only for the VCLES and CLES grids. The values of invariants were of the order of $I_1, I_2, I_3 \sim -10^{-9}$ at the grid points at which the violation occurred. Correspondingly, these violations are of the order of numerical errors in simulations and not due to the unified model.

6.2. Limits of the Unified Model

The LUM introduced in Sect. 3 describes continuous variations between the DNS, LES and RANS scale. After developing a corresponding computational method for the LUM, the question arises of how the DNS and RANS limits are realized by the computational method. Regarding the large Δ limit there is the question of whether the computational method applying the DC coupling approach results in a RANS method for a large filter width Δ. Regarding the small Δ limit there is the question of how the DNS limit is realized. In particular, there is the question of whether the DNS scaling obtained with the filter width Δ defined by the large side filter provides a DNS scaling in consistency with theoretical analyses [98]. These questions about the limits of the computational method will be addressed here regarding the use of the LUM in simulations.

The transition from DNS to the LES and RANS scales is illustrated in Fig. 10 which shows the ratio $r_k = k/(k + k_{res})$ of the modeled turbulent kinetic energy to the total kinetic energy along the wall-normal direction, where k_{res} refers to the resolved turbulent kinetic energy. Hence, the DNS limit ($r_k = 0$) and RANS limit ($r_k = 1$) are obtained everywhere in the domain if the grid is sufficiently fine or coarse, respectively. However, on fine grids there will be a difference between the filtered velocity $\widetilde{U}$ obtained from the unified simulation and the velocity field U obtained from DNS without using any turbulence model. Correspondingly, on coarse grids there will be a difference between $\widetilde{U}$ obtained from a unified simulation and the mean velocity obtained by using a pure RANS model. These differences depend on r_k. An empirical expression which provides a relation between Δ and r_k is a useful tool for the construction of grids for unified simulations. For example, such a relation can be used to account for grid requirements in certain flow regions (e.g., to ensure that LES is performed in a transitional flow region). The variation of the peak value r_{kp} of r_k with the filter width Δ is shown in Fig. 11. Here, r_k was calculated as in Fig. 10 by considering the anisotropy function (26). The value of Δ refers to the maximum of Δ provided by the large side filter without using the anisotropy function. Thus, there is one Δ value per grid. The following exponential fit is considered to quantify the variation of r_{kp} with the filter width Δ,

$$r_{kp} = \left[1 - \exp\left(-\alpha \Delta^{\beta}\right)\right]^{4/\beta}, \tag{31}$$

where α and β are model constants. This equation structure ensures that we recover $r_{kp} \sim \Delta^4$ in the small-Δ limit in agreement with the corresponding theoretical estimate obtained by Pope [98]. The values of the constants were calculated by minimizing the error between the r_{kp} values observed in simulations and the corresponding r_{kp} values calculated by means of Eq. (31). The minimal L2 error was found to be 0.027% for the values $\alpha = 4.84$ and $\beta = 0.53$. The comparison between the simulation data and the numerical fit (31) is shown in Fig. 11. It can be seen that the empirical fit provides a very good approximation to the data over the entire range of r_{kp} values.

7. *A Posteriori* Analysis of Model Accuracy

The accuracy of the LUM will be investigated in this section. In particular, the performance of the LUM will be compared with the performance of the DES model [51] and pure LES, and the influence of the RANS model applied as part of the LUM will be studied. The analyses presented below are organized in the following way. In Sect. 7.1, LUM results will be compared to pure LES and DES results by using DNS data (see also the next paragraph) for the evaluation of the model performance. These comparisons will be performed for the $Re_\tau = 395$ and $Re_\tau = 2000$ cases by using the LES grid. This grid is usually considered to be appropriate for performing LES at $Re_\tau = 395$ [95], and it is very coarse for simulations at $Re_\tau = 2000$. The simulation at $Re_\tau = 395$ will demonstrate that the LUM and DES performance is similar to LES on fine grids. The simulation at $Re_\tau = 2000$ will demonstrate the deficiencies of LES on coarse grids in comparison to hybrid models. To see the differences between the LUM, DES, and a two-equation hybrid model based on renormalization group (RNG) theory [31], which will be referred to as renormalization group model (RNGM), we will also present model results obtained on the VFLES grid for $Re_\tau = 5000$. The domain and resolution of the VFLES grid are chosen in accordance with the DES simulations of Keating and Piomelli [56] and the RNGM simulations of De Langhe et al. [31]. No LES is performed at this Reynolds number, because it is computationally too expensive. In Sect. 7.2, the influence of the RANS model used as ingredient of the LUM will be considered. This will be done for the $Re_\tau = 2000$ case, which is the highest Reynolds number case for which DNS data are available for comparisons, by using the LES grid to see the difference to the corresponding comparisons of unified and DES models. The domain sizes applied for these simulations at different Re_τ are given in Table 1. The grids applied are defined in Table 2.

DNS data for $Re_\tau = 395$ obtained by using a spectral code, which were proven to agree very well with the corresponding DNS data of Moser et al. [90], for $Re_\tau = 590$ [90], and for $Re_\tau = 2000$ [99] are used here for comparisons. However, DNS data are not available for the validation of unified simulations beyond $Re_\tau = 2000$. In order to validate unified simulation results at higher friction Reynolds numbers, the empirical mean streamwise velocity profile of Reichardt [100] has been often applied. This relation is given by [100]

$$U^+ = \frac{1}{\kappa}\ln(1+\kappa y^+) + 7.8\left[1 - \exp\left(-\frac{y^+}{11}\right) - \frac{y^+}{11}\exp\left(-\frac{y^+}{3}\right)\right], \tag{32}$$

where $U^+ = \widetilde{U}_1/u_\tau$ is the dimensionless mean streamwise velocity. A plot of U^+/y^+ obtained from DNS for different friction Reynolds numbers is shown in Fig. 12a . It can be seen that there is a very good agreement between the curves for different Re_τ. The empirical fit (32) of Reichardt was obtained on the basis of experimental data [100].

To obtain the best possible agreement between the DNS data shown in Fig. 12a and the profile of Reichardt, we generalize Eq. (32) by the function

$$U^+ = \frac{1}{\kappa}\ln(1+\kappa y^+) + A\left[1 - \exp\left(-\frac{y^+}{T_1}\right) - \frac{y^+}{T_1}\exp\left(-\frac{y^+}{T_2}\right)\right]^p . \qquad (33)$$

This expression involves the four unknowns A, T_1, T_2, and p. The values of A and T_1 were fixed by the requirement that Eq. (33) agrees exactly with two points of the $Re_\tau = 2000$ curve given in Fig. 12a. These two points are chosen close to $y^+ = 10$ and $y^+ = 30$, respectively. The values of the constants T_2 and p were obtained by minimizing the quadratic error between the DNS velocity data and the corresponding values provided by Eq. (33). In this way, we found $T_2 = 4.25$ and $p = 0.96$. The resulting modified empirical velocity fit is then given by

$$U^+ = \frac{1}{\kappa}\ln(1+\kappa y^+) + 7.31\left[1 - \exp\left(-\frac{y^+}{7.87}\right) - \frac{y^+}{7.87}\exp\left(-\frac{y^+}{4.25}\right)\right]^{0.96} . \qquad (34)$$

The plot of the new empirical fit (which will be referred to as Reichardt profile below) is compared with the DNS data in Fig. 12b for the $Re_\tau = 2000$ case. It can be seen that the new fit provides an excellent agreement with the DNS data. The L2 norm of the deviations between the $Re_\tau = 2000$ DNS results for the mean velocity and the profile given by Eq. (34) was found to be smaller than 0.019%.

7.1. Comparisons with LES and DES

Figure 13 shows a comparison of the mean streamwise velocity and total turbulent kinetic energy obtained with LES, DES, the LUM and DNS [90] at $Re_\tau = 395$. Both, the mean velocity profiles and total turbulent kinetic energy profiles predicted by the three models are almost identical. It can thus be concluded that the unified simulation recovers the LES limit if the grid is sufficiently fine. In comparison to the DNS data, a slight overprediction of the mean velocity starting at $y^+ \approx 30$ can be observed in all three simulations. The peak of the turbulent kinetic energy profile is also overpredicted in all three simulations. The use of the wall-normal grid resolution applied in the second-order finite volume method is too coarse to achieve a better agreement with DNS results [101]. By repeating these simulations by using the FLES grid instead of the LES grid, it was proven that the overprediction of the mean velocity basically disappears (not shown).

To evaluate the model performances at higher Reynolds numbers, the comparison between the three methods and DNS data is shown in Fig. 14 for the $Re_\tau = 2000$ case. The results show that LES provides very poor predictions of the mean streamwise velocity and total turbulent kinetic energy. The mean velocity profile predicted by DES shows a deviation from the DNS results in the viscous and buffer region and eventually in the log-law region. The unified model predicts the mean velocity in the viscous and buffer regions in close agreement with DNS. The overprediction of the velocity towards the channel center is slightly smaller than in the DES results. For the total kinetic energy the LUM provides again improved results as compared to DES: the peak value is predicted in close agreement with DNS data and the sharp decrease after the peak is predicted much better by the LUM than by the DES model. It should be noted that the predictions of the DES model could probably be improved by using empirical modifications, as proposed by Spalart et al. [35].

To understand the reason for the poor performance of LES on a coarse grid, we consider the plot of the total turbulent kinetic energy for the $Re_\tau = 2000$ case. On a coarse grid, the characteristic length scale L of large turbulence structures is much smaller than the filter width in the near-wall region. Hence, the use of the filter width as the length scale does not capture the information contained in the large-scale turbulence structures. The transport equation for k given by Eq. (3) involves two source terms: the turbulence production term $P = -D_{ij}\partial\widetilde{U}_j/\partial x_i \sim f(\Delta)$ and the turbulent dissipation term ϵ, which is given in LES by $\epsilon = k^{3/2}/\Delta$. On coarse grids, the large value of Δ causes an increase of the turbulence production P and a decrease of the SGS dissipation ϵ. Thus, the ratio P/ϵ becomes very high in the near wall region, which leads to a significant increase of the total turbulent kinetic energy. Hence, the use of the filter width as the length scale in the near-wall region is the reason for the inaccurate predictions of pure LES on coarse grids. The LUM overcomes this problem by modeling the near-wall region on coarse grids with a RANS method based on a flow dependent length scale, which results in improved predictions of flow statistics in the near-wall region.

The discussion above in this section has shown that both the LUM and DES produce results comparable to LES on fine grids, and more accurate results than LES on coarse grids. Moreover, a slightly better performance of the LUM could be observed for the higher $Re_\tau = 2000$ case. Both, unified and DES models are designed to be used for high Reynolds number flow simulations. Therefore, it is interesting to compare the two models for even higher Reynolds numbers than $Re_\tau = 2000$. Accordingly, additional simulations have been performed with the unified and DES models at a friction Reynolds number of $Re_\tau = 5000$ by using the VFLES grid. The location of the LES-RANS interface has been shown to affect simulation results of DES and hybrid methods [31]. Hence, it is important to have the same interface location when comparing DES and other hybrid models. The latter was accomplished in the following way. In DES, the location of the interface is determined by $C_{DES}\Delta = y$, which defines the switch of the length scale applied according to $\widetilde{d} = \min(C_{DES}\Delta, y)$. The filter width is calculated by using the large side filter, such that the value of Δ is constant throughout the domain and known. The unified simulation showed that the location of the RANS-LES interface was at $y^+ \approx 96$, which determines y. The use of the corresponding values of Δ and y in $C_{DES}\Delta = y$ then results in $C_{DES} = 0.38$.

The mean streamwise velocity profiles obtained with the LUM and DES are compared to the empirical profile (34) in Fig. 15a. Also shown in this figure are the data of the mean velocity profile obtained by using the RNGM [31], for which the RANS-LES interface is located at $y^+ \approx 100$. The mean velocity predicted by the RNGM only agrees with the DNS data up to $y^+ \approx 20$. For $20 < y^+ < 700$, a significant underprediction is observed, and the velocity is overpredicted for $y^+ > 700$. The LUM and DES results almost identically agree with the Reichardt profile up to the RANS-LES interface location $y^+ \approx 96$. Beyond the interface, the LUM results continue to agree well with the Reichardt profile up to $y^+ = 300$, while the DES results display a mismatch of the velocity in the log-law region, as it was also reported by Keating and Piomelli [56]. This observed mismatch induces higher errors in the prediction of the skin-friction coefficient $C_f = \tau_w/(0.5\rho U_b^2)$, where U_b refers to the bulk velocity. For the simulations considered here, the error $E_{Cf} = 100\,(C_f - C_{f,Dean})/C_{f,Dean}$ in the prediction of the skin-friction coefficient (in comparison with Dean's empirical skin-friction coefficient $C_{f,Dean} = 0.073(2U_b\delta/\nu)^{-1/4}$ obtained from experiments [102]) was found to be -9.8%, -15.5% and 16.5% for the LUM, DES and RNGM models, respectively.

To understand the reason for the improved mean velocity profile and skin-friction coefficient obtained by the LUM, comparisons of the Reynolds shear stress (modeled and resolved) and turbulent viscosity obtained from LUM and DES simulations are shown in Figs. 15b and 15c, respectively. In the RANS region between the wall and the interface, the modeled shear stress is much larger than the resolved shear stress. Both models have been designed to accurately predict the shear stress in the RANS mode. Thus, the results obtained from both models are very similar. Beyond the interface location, the modeled shear stress gradually reduces, while the resolved shear stress increases. Fig. 15c shows that the turbulent viscosity obtained from DES is significantly smaller near the interface than the turbulent viscosity obtained from the LUM. This difference is due to the different methods used to calculate the turbulent viscosity. Because both models predict the same value for the modeled shear stress $R_{xy} \approx -\langle\nu_t\rangle\partial\langle\tilde{U}\rangle/\partial y$ at the interface but DES predicts a smaller turbulent viscosity, $\langle\nu_t\rangle^{DES} < \langle\nu_t\rangle^{LUM}$, we have $(\partial\langle\tilde{U}\rangle/\partial y)^{DES} > (\partial\langle\tilde{U}\rangle/\partial y)^{LUM}$. The mean velocity gradient is thus too large in DES near the interface, which implies that the mean velocity predicted by DES deviates from the log-law. This overprediction of the velocity gradient is an inherent issue of DES, which cannot be removed by adjusting the model constant C_{DES} [56].

The comparisons between the LUM, DES, and RNGM presented above lead to two relevant conclusions. First, the LUM provides the most accurate prediction of the skin-friction coefficient among the three models considered. Second, in difference to the other two models considered, the LUM provides predictions which agree with the log-law over a wide range of y^+ values. This agreement is observed for about 50% of the log-law region. On the other hand, the DES shows an agreement with the log-law over only about 25% of the log-law region, and the RNGM does not agree at all with the log-law. The facts (i) that most hybrid models are similar to DES [26] and (ii) corresponding validations of the performance of other hybrid methods are unavailable for such a high Reynolds number case support the view that the LUM performs better than other (comparably simple) linear hybrid models. It has to be noted that there are ways to improve the performance of hybrid methods with regard to channel flow simulations: the addition of fluctuations or an additional filtering of the velocity field near the RANS-LES interface have been proven to overcome the log-law mismatch problem [35, 56, 57]. However, the suitability of such flow-dependent problem solutions for other applications is unclear. A more general solution to this problem may be obtained by combinations of hybrid RANS-LES methods with dynamic LES methods implied by stochastic analysis [103].

7.2. Influence of RANS Models

The previous section demonstrates the advantages of the LUM compared to LES and DES. In this subsection, it will be shown that the advantages of the LUM do not depend on a particular choice of the RANS model. To address the latter question, unified RANS-LES simulations were performed on the LES grid for $Re_\tau = 2000$ by using two RANS models. The first RANS model is the $k - \omega$ model described in Sect. 3. This model is known to provide accurate RANS predictions of channel flow. The second RANS model is the one-equation model of Wolfshtein [104], which uses a transport equation for the turbulent kinetic energy where the dissipation rate is closed in terms of an empirical expression for the characteristic length scale of large-scale turbulent motions. Wolfshtein's model is known to be not very accurate for channel flow (see also Fig. 16). Regarding the numerical implementation of both models, the only difference between the $k - \omega$ model and Wolfshtein's model is the different calculation of the RANS time scale τ^{RANS}.

A comparison of the results for the mean streamwise velocity obtained with the two models and DNS data is shown in Fig. 16. The results obtained using the one-equation model in pure RANS mode show a significant underprediction of the mean velocity compared to DNS. However, when used as part of the unified RANS-LES method, the one-equation model performs equally well as the unified method based on a two-equation RANS model. Compared to DNS, the error in the prediction of the skin-friction coefficient was 3% and 4% for the unified model combined with the two-equation $k-\omega$ model and the one-equation model of Wolfshtein, respectively. On the other hand, the use of the one-equation model in pure RANS mode resulted in an error of 35% in the prediction of the skin-friction coefficient. Hence, it can be concluded that the choice of the RANS model used in the near-wall region does not significantly affect the accuracy of numerical predictions of the unified method using a time-scale based RANS-LES transition in channel flows. However, further testing of unified RANS-LES models for complex flows (abrupt expansion, curved boundaries, dynamic stall, etc.) is needed to verify the generality of this conclusion.

8. *A Posteriori* Analysis of Model Cost

Unified RANS-LES methods are not only more accurate than LES on coarse grids, but they are also much more efficient. This computational efficiency will be quantified in this section on the basis of a computational cost analysis of the LUM. The cost of unified simulations are determined by the relative amount of modeled energy $r_k = k/(k_{res}+k)$, where k_{res} is the resolved turbulent kinetic energy. This parameter is a function of the normalized wall-normal distance y/δ, the Reynolds number, and the number N of grid points applied,

$$r_k = g(y/\delta, Re, N), \tag{35}$$

see, for example, Fig. 10. The use of this formula for the calculation of the number of grid points N required for unified RANS-LES simulations requires the specification of a global value of r_k, so that N can be calculated in dependence on this global value and Re. We will use here the bulk value

$$R_k = \frac{1}{\delta}\int_0^\delta r_k dy \tag{36}$$

as a characteristic value for r_k, where δ is the half-channel width. Then, Eq. (35) can be written

$$R_k = G(Re, N), \tag{37}$$

where G refers to an unknown function. This equation can be reformulated as an equation for the number of grid points required in unified simulations,

$$N = F(Re, R_k), \tag{38}$$

where F refers to a function that has to be specified. For the following it is helpful to specify this formula in the following way,

$$\ln N = a(R_k) \ln Re + b(R_k). \tag{39}$$

Justification for this assumption arises from the fact that computational cost estimates for DNS and LES, which correspond to a constant R_k, reveal a power-law dependence on the Reynolds number $\ln N \sim C \ln Re$ [2, 24].

Unified simulations were performed at seven Reynolds numbers Re ranging from 5640 to 542000 (corresponding to $Re_\tau = (180,\ 395,\ 590,\ 950,\ 2000,\ 5000,\ 10000)$). The relation $Re_\tau = 0.09 Re^{0.88}$ [2] was used to relate Re_τ to Re. For each of the seven Reynolds numbers considered, simulations were performed on five grids (RANS, VVVCLES, VCLES, CLES, LES). The data obtained from these simulations are shown in Fig. 17a. Next, for each Re value, the available $N(R_k)$ values were used to obtain a linear interpolation for $N(R_k)$. This interpolation was used to calculate the values of N at the values $R_k = 0.2, 0.4, 0.6,$ and 0.8. The interpolated data points obtained in this way are shown in Fig. 17b. These data demonstrate the suitability of applying the linear function (39). At each $R_k = 0.2, 0.4, 0.6,$ and 0.8 considered, the Fig. 17b data points can be used to determine $a(R_k)$ and $b(R_k)$ values according to Eq. (39). The resulting $a(R_k)$ and $b(R_k)$ values are shown in Fig. 18. To obtain analytical functions for $a(R_k)$ and $b(R_k)$, linear curve fitting was applied to produce the lines in Fig. 18. It may be seen that these linear curves represent the variation of $a(R_k)$ and $b(R_k)$ with R_k very well. The curves obtained are given by $a(R_k) = 2.53 - 2.29 R_k$ and $b(R_k) = 13.36 R_k - 10.76$. The use of the latter two relations in Eq. (39) results in

$$N = e^{13.36 R_k - 10.76} Re^{2.53 - 2.29 R_k}. \tag{40}$$

The implications of Eq. (40) are illustrated by the lines in Fig. 17b. It may be seen that the cost formula (40) agrees very well with the available data. The DNS ($R_k = 0$) and RANS ($R_k = 1$) curves that follow from Eq. (40) are also shown in Fig. 17b. In the DNS limit, Eq. (40) provides a scaling of $N \sim Re^{2.53}$, which agrees well with the estimate $N \sim Re^{2.7}$ cited by Pope [2] for channel flow. In the RANS limit, Eq. (40) provides a scaling of $N \sim Re^{0.24}$. Hence, the RANS cost are not strongly affected by the Reynolds number, which agrees well with other observations [2, 18]. In the LES limit we apply $R_k = 0.2$. Equation (40) provides then an LES scaling of $N \sim Re^{2.07}$. This scaling is comparable to the previous LES cost estimate $N \sim Re^{1.76}$ for wall-bounded flows [24].

To compare the computational cost of LES with the cost of unified simulations we have to specify a characteristic value of R_k used for unified simulations. For doing this, the value $R_k = 0.4$ is chosen due to three reasons: (i) the accuracy of predictions is still comparable to LES, (ii) higher values of R_k cause the solution to become RANS because turbulent fluctuations vanish, (iii) $R_k = 0.4$ is often used in hybrid RANS-LES simulations using partially-averaged Navier-Stokes methods [32, 67]. By comparing the cost of LES ($R_k = 0.2$) with the cost of unified simulations ($R_k = 0.4$) we obtain according to Eq. (40)

$$\frac{N_{LES}}{N_{Unified}} = (e^{-13.36}\, Re^{2.29})^{0.2} = 0.07\, Re^{0.46}. \tag{41}$$

The corresponding computational cost ratio is shown in Fig. 19. At relatively low Reynolds numbers, there is no significant advantage related to the use of the unified model. However, at these Reynolds numbers it is not very expensive to perform LES. At relatively high Reynolds numbers, there is a significant advantage related to the use of unified models. The gain at higher Reynolds numbers can be demonstrated by the following example. The LES of the flow field around an actual wind turbine requires around 30 million grid points. The Reynolds numbers of the atmospheric flow around the wind turbine is about $Re \sim 10^9$. For this Reynolds number, the LES to unified cost ratio given by Eq. (41) is 966. Therefore, unified simulations can be performed by using about 31000 grid points. Such cost reductions enable simulations of complex flows which are not feasible otherwise.

9. Summary

The motivation of the introduction of hybrid RANS-LES methods is a computational cost reduction of LES by orders of magnitudes. However, a huge variety of hybrid RANS-LES models are currently in use such that there is the question of which hybrid RANS-LES method represents the optimal approach. This question matters because there are significant accuracy and cost differences between different hybrid RANS-LES methods [27]. The properties of an optimal hybrid RANS-LES model were formulated here by taking reference to fundamental properties of fluid flow equations. It was shown that the unified RANS-LES model derived by Heinz [33] from an underlying stochastic turbulence model has the properties of an optimal hybrid RANS-LES model. This conclusion leads to three relevant questions, which will be addressed in the following three paragraphs.

The first question is whether the computational realization of the theoretically derived unified RANS-LES model also has the properties of an optimal hybrid RANS-LES model. The computational efficiency of unified RANS-LES models depends significantly on the way in which RANS and LES equations are coupled. The suitability of three coupling methods was investigated here regarding the LUM by *a priori* analyses of channel flow data. It was shown that the DC coupling approach, which uses RANS and LES equations dynamically, represents the most convenient approach. The coupling analyses were also used to computationally develop unified RANS-LES methods by determining the most appropriate filter width and transfer function definitions. It is worth noting that the numerical implementation of the LUM is straightforward and requires only minor modification of existing methods. *A posteriori* analyses of channel flow data were used then to demonstrate that the computational model obtained in this way does also satisfy the properties of an optimal hybrid RANS-LES model. It was shown that the stress tensor of the LUM satisfies the realizability requirement to be non-negative definite. It was also shown that the LUM varies continuously between the DNS, LES, and RANS limits. The influence of choosing the computational grid on the (DNS, LES, and RANS) nature of the model applied was specified in terms of the scaling relation (31).

The second question is whether simulations using the optimal hybrid RANS-LES method applied here have advantages compared to simulations performed with other computational methods. Compared to RANS simulations, the LUM has significant advantages. RANS simulations are known to require evidence for their predictions. However, such evidence is often simply unavailable because of the lack of experimental or DNS data. On the other hand, the LUM is relatively independent of the RANS model applied (see Sect. 7.2). Without adjustments to the flow considered, the LUM can provide predictions that agree well with DNS data. Compared to LES, the LUM also has significant advantages. One advantage is the huge cost reduction of high-Reynolds number simulations by a factor of $0.07\,Re^{0.46}$. Another advantage is the significant accuracy advantage compared to LES with regard to simulations on coarse grids (as usually required for atmospheric boundary layer simulations). Compared to other hybrid methods, the LUM also has advantages. The comparisons with the RNGM and DES in Sect. 7.1 showed that the LUM provides the most accurate prediction of the skin-friction coefficient, and, in difference to the RNGM and DES, the LUM provides predictions which agree with the log-law over a wide range of y^+ values. As discussed at the end of Sect. 7.1, there are at least indications that the LUM also performs better than other (comparably simple) linear hybrid models.

The third question is whether the optimal hybrid RANS-LES method applied here represents a general method, which can be used for accurate and efficient simulations of a broad range of turbulent flows. Regarding this question it is relevant to note that simulations of a variety of swirling turbulent jet flows (involving vortex breakdown at high swirl numbers) also revealed the excellent performance of the LUM [76]. On the other hand, DES is known to be not well appropriate for jet-like flows [19, 105], such that DES calculations of swirling jet flows suffer from problems [106, 107]. It is also relevant to note that (depending on the needs) the hybrid RANS-LES method presented here can be extended and modified in several ways. Extensions are possible by involving a quadratic stress model or stress transport equation [33]. Another extension is the incorporation of a dynamic method for performing LES in the unified RANS-LES method [83, 103]. Modifications are possible via the choice of the coupling approach used to perform unified RANS-LES simulations. The DC approach was found to be the most appropriate coupling approach for the attached flow considered. However, the use of the FC approach may also be of interest for applications. For certain flows, it is essential to model a portion of the domain using LES because unsteadiness is required (e.g., for aeroacoustic noise predictions). The DC approach can also be used for separated flows. However, when the grid resolution causes the RANS-LES interface to be located within the turbulent boundary layer, the LES region can induce early flow separation, referred to as grid induced separation [26, 35]. This problem can be circumvented when the entire boundary layer is modeled using RANS, and the interface is located outside the boundary layer [26, 35]. When the DC approach cannot ensure that the entire boundary layer is in RANS mode, the FC approach should be used instead. For this case, the EC approach, which is the exact approach implied by theory, can be used to confirm the validity of the FC approach (see the discussion of the grid dependence of the FC approach in the first paragraph of Sect. 5.3).

Acknowledgments

The authors would like to acknowledge support for this work through a gift from BP Alternative Energy North America Inc to the UW Wind Energy Research Center. Additional support from the UW School of Energy Resources is also gratefully acknowledged. This work was partially supported by the UW Institute for Scientific Computation. The authors would like to thank Dr. John Gibson for helpful discussions regarding the use of the DNS code. S. Heinz would like to acknowledge partial support through NASA’s NRA research opportunities in aeronautics program (Grant No. NNX12AJ71A) with Dr. P. Balakumar as the technical officer. We would like to thank the referees for their very helpful suggestions for improvements.

References

[1] W. Reynolds, The potential and limitations of direct and large eddy simulations, in: L. Lumley (Ed.), Whither Turbulence? Turbulence at the Crossroads, vol. 357 of *Lecture Notes in Physics*, Proceedings of a Workshop Held at Cornell University, Ithaca, NY, 313–343, 1989.

[2] S. B. Pope, Turbulent Flows, Cambridge University Press, Cambridge, 2000.

[3] C. Meneveau, Statistics of turbulence subgrid-scale stresses: Necessary conditions and experimental tests, Physics of Fluids 6 (1994) 815–833.

[4] P. J. Mason, Large-eddy simulation: A critical review of the technique, Quarterly Journal of the Royal Meteorological Society 120 (1994) 1–26.

[5] M. Germano, Fundamentals of large eddy simulation, in: K. E. Peyret, R. (Ed.), Advanced Turbulent Flows Computations, vol. 395 of *CISM Courses and Lectures*, Springer, Berlin, Heidelberg, New York, 81–130, 2000.

[6] U. Piomelli, Large-eddy simulation: achievements and challenges, Progress in Aerospace Sciences 35 (1999) 335–362.

[7] C. Meneveau, J. Katz, Scale-invariance and turbulence models for large-eddy simulation, Annual Review of Fluid Mechanics 32 (2000) 1–32.

[8] P. Sagaut, Large Eddy Simulation for Incompressible Flows: An Introduction, Springer-Verlag, Berlin, Heidelberg, New York, Tokyo, 2002.

[9] M. Lesieur, O. Metais, P. Comte, Large-Eddy Simulations of Turbulence, Cambridge University Press, Cambridge, 2005.

[10] P. J. Colucci, F. A. Jaberi, P. Givi, S. B. Pope, Filtered density function for large eddy simulation of turbulent reacting flows, Physics of Fluids 10 (1998) 499–515.

[11] F. A. Jaberi, P. J. Colucci, S. James, P. Givi, S. B. Pope, Filtered mass density function for large-eddy simulation of turbulent reacting flows, Journal of Fluid Mechanics 401 (1999) 85–121.

[12] L. Gicquel, P. Givi, F. Jaberi, S. Pope, Velocity filtered density function for large eddy simulation of turbulent flows, Physics of Fluids 14 (2002) 1196–1213.

[13] M. R. H. Sheikhi, T. G. Drozda, P. Givi, S. B. Pope, Velocity-scalar filtered density function for large eddy simulation of turbulent flows, Physics of Fluids 15 (2003) 2321–2337.

[14] S. Heinz, On Fokker-Planck equations for turbulent reacting flows. Part 2. Filter density function for large eddy simulation, Flow, Turbulence and Combustion 70 (2003) 153–181.

[15] P. Givi, Filtered density function for subgrid scale modeling of turbulent combustion, AIAA Journal 44 (2006) 16–23.

[16] M. Sheikhi, P. Givi, S. Pope, Velocity-scalar filtered mass density function for large eddy simulation of turbulent reacting flows, Physics of Fluids 19 (2007) 095106:1–21.

[17] M. Sheikhi, P. Givi, S. Pope, Frequency-velocity-scalar filtered mass density function for large eddy simulation of turbulent flows, Physics of Fluids 21 (2009) 075102:1–14.

[18] K. Hanjalić, Advanced turbulence closure models: a view of current status and future prospects, International Journal of Heat and Fluid Flow 15 (1994) 178–203.

[19] D. C. Wilcox, Turbulence Modeling for CFD, DCW Industries, Canada, 2nd edn., 1998.

[20] S. Heinz, On Fokker-Planck equations for turbulent reacting flows. Part 1. Probability density function for Reynolds-averaged Navier–Stokes equations, Flow, Turbulence and Combustion 70 (2003) 115–152.

[21] S. Heinz, Statistical Mechanics of Turbulent Flows, Springer-Verlag, Berlin, Heidelberg, New York, Tokyo, 1st edn., 2003.

[22] R. Fox, Computational Models for Turbulent Reacting Flows, Cambridge University Press, Cambridge, 2003.

[23] K. Hanjalić, Will RANS survive LES?: A view of perspectives, Journal of Fluids Engineering 127 (2005) 831–839.

[24] D. R. Chapman, Computational aerodynamics development and outlook, AIAA Journal 17 (1979) 1293–1313.

[25] J. S. Baggett, On the feasibility of merging LES with RANS for the near-wall region of attached turbulent flows, Annual Research Briefs, Center for Turbulence Research, NASA Ames/Stanford University (1998) 267–277.

[26] P. R. Spalart, Detached-eddy simulation, Annual Review of Fluid Mechanics 41 (2009) 181–202.

[27] J. Fröhlich, D. V. Terzi, Hybrid LES/RANS methods for the simulation of turbulent flows, Progress in Aerospace Sciences 44 (2008) 349–377.

[28] K. Squires, Detached-eddy simulation: current status and perspectives, in: Direct and Large-Eddy Simulation V: Proceedings of the fifth international ERCOFTAC Workshop on Direct and Large-eddy Simulation, Springer Netherlands, Munich University of Technology, Munich, Germany, 465, 2003.

[29] M. Germano, Properties of the hybrid RANS/LES filter, Theoretical and Computational Fluid Dynamics 17 (2004) 225–231.

[30] C. De Langhe, B. Merci, E. Dick, Hybrid RANS/LES modelling with an approximate renormalization group. I: Model development, Journal of Turbulence 6 (2005) 1–18.

[31] C. De Langhe, B. Merci, K. Lodefier, E. Dick, Hybrid RANS/LES modelling with an approximate renormalization group. II: Applications, Journal of Turbulence 6 (2005) 1–16.

[32] S. Girimaji, Partially-averaged Navier-Stokes model for turbulence: a Reynolds-averaged Navier-Stokes to direct numerical simulation bridging method, Journal of Applied Mechanics 73 (2006) 413–421.

[33] S. Heinz, Unified turbulence models for LES and RANS, FDF and PDF simulations, Theoretical and Computational Fluid Dynamics 21 (2007) 99–118.

[34] M. Sánchez-Rocha, S. Menon, The compressible hybrid RANS/LES formulation using an additive operator, Journal of Computational Physics 228 (2009) 2037–2062.

[35] P. R. Spalart, S. Deck, M. L. Shur, K. D. Squires, M. K. Strelets, A. Travin, A new version of detached-eddy simulation, resistant to ambiguous grid densities, Theoretical and Computational Fluid Dynamics 20 (2006) 181–195.

[36] M. Breuer, B. Jaffrézic, K. Arora, Hybrid LES-RANS technique based on a one-equation near-wall model, Theoretical and Computational Fluid Dynamics 22 (2008) 157–187.

[37] L. Davidson, S. H. Peng, Hybrid LES-RANS modelling: a one-equation SGS model combined with a k-ω model for predicting recirculating flows, International Journal for Numerical Methods in Fluids 43 (2003) 1003–1018.

[38] F. Hamba, A hybrid RANS/LES simulation of turbulent channel flow, Theoretical and Computational Fluid Dynamics 16 (2003) 387–403.

[39] P. Spalart, Direct simulation of a turbulent boundary layer up to $R_\theta = 1410$, Journal of Fluid Mechanics 187 (1988) 61–98.

[40] T. S. Lund, X. Wu, K. D. Squires, Generation of turbulent inflow data for spatially-developing boundary layer simulations, Journal of Computational Physics 140 (1998) 233–258.

[41] S. Stolz, N. A. Adams, Large-eddy simulation of high-Reynolds-number supersonic boundary layers using the approximate deconvolution model and a rescaling and recycling technique, Physics of Fluids 15 (2003) 2398–2412.

[42] P. Druault, S. Lardeau, J. P. Bonnet, F. Coiffet, J. Delville, E. Lamballais, J. F. Largeau, L. Perret, Generation of three-dimensional turbulent inlet conditions for large-eddy simulation, AIAA Journal 42 (2004) 447–456.

[43] J. U. Schluter, H. Pitsch, P. Moin, Large Eddy Simulation inflow conditions for coupling with Reynolds-averaged flow solvers, AIAA Journal 42 (2004) 478–484.

[44] K. Liu, R. H. Pletcher, Inflow conditions for the large eddy simulation of turbulent boundary layers: A dynamic recycling procedure, Journal of Computational Physics 219 (2006) 1–6.

[45] S. McIlwain, A. Pollard, Large eddy simulation of the effects of mild swirl on the near field of a round free jet, Physics of Fluids 14 (2002) 653–661.

[46] M. Garcıa-Villalba, J. Fröhlich, W. Rodi, On inflow boundary conditions for large eddy simulation of turbulent swirling jets, in: Proc. 21st Int. Congress of Theoretical and Applied Mechanics. Warsaw. Poland, 2004.

[47] C. P. Zemtsop, M. K. Stöllinger, S. Heinz, D. Stanescu, Large eddy simulation of swirling turbulent jet flows in absence of vortex breakdown, AIAA Journal 47 (2009) 3011–3021.

[48] P. Quemere, P. Sagaut, V. Couailler, A new multi-domain/multi-resolution method for large-eddy simulation, International Journal for Numerical Methods in Fluids 36 (2001) 391–416.

[49] D. V. Terzi, J. Fröhlich, Coupling conditions for LES with downstream RANS for the prediction of incompressible turbulent flows, in: Proc. of 5th Int. Symp. on Turbulence and Shear Flow Phenomena TSFP, vol. 5, 765–770, 2007.

[50] A. Smirnov, S. Shi, I. Celik, Random flow generation technique for large eddy simulations and particle-dynamics modeling, Journal of Fluids Engineering 123 (2001) 359–371.

[51] P. Spalart, W. Jou, M. Strelets, S. Allmaras, Comments on the feasibility of LES for wings, and on a hybrid RANS/LES approach, in: 1st AFOSR Intl. Conf. on DNS/LES, Columbus: Greyden Press, Ruston, LA, USA, 4–8, 1997.

[52] A. Travin, M. Shur, M. Strelets, P. Spalart, Detached-eddy simulations past a circular cylinder, Flow, Turbulence and Combustion 63 (2000) 293–313.

[53] L. S. Hedges, A. K. Travin, P. R. Spalart, Detached-eddy simulations over a simplified landing gear, Journal of Fluids Engineering 124 (2002) 413–423.

[54] P. G. Tucker, L. Davidson, Zonal k–l based large eddy simulations, Computers and Fluids 33 (2004) 267–287.

[55] F. Tessicini, L. Temmerman, M. A. Leschziner, Approximate near-wall treatments based on zonal and hybrid RANS–LES methods for LES at high Reynolds numbers, International Journal of Heat and Fluid Flow 27 (2006) 789–799.

[56] A. Keating, U. Piomelli, A dynamic stochastic forcing method as a wall-layer model for large-eddy simulation, Journal of Turbulence 7 (2006) 1–24.

[57] F. Hamba, Log-layer mismatch and commutation error in hybrid RANS/LES simulation of channel flow, International Journal of Heat and Fluid Flow 30 (2009) 20–31.

[58] B. Kniesner, S. Šarić, A. Mehdizadeh, S. Jakirlić, K. Hanjalić, C. Tropea, et al., Wall treatment in LES by RANS models: Method development and application to aerodynamic flows and swirl combustors, ERCOFTAC Bulletin 72 (2007) 33–40.

[59] C. G. Speziale, Turbulence modeling for time-dependent RANS and VLES: a review, AIAA Journal 36 (1998) 173–184.

[60] H. Zhang, C. Bachman, H. Fasel, Application of a new methodology for simulations of complex turbulent flows, in: Fluids 2000 Conference and Exhibit, Denver, CO, 2000.

[61] H. F. Fasel, D. A. V. Terzi, R. D. Sandberg, A methodology for simulating compressible turbulent flows, Journal of Applied Mechanics 73 (2006) 405–412.

[62] J. Sivasubramanian, R. D. Sandberg, D. A. von Terzi, H. F. Fasel, Numerical investigation of transitional supersonic base flows with flow control, Journal of Spacecraft and Rockets 44 (2007) 1021–1028.

[63] P. Sagaut, M. Germano, On the filtering paradigm for LES of flows with discontinuities, Journal of Turbulence 6 (2005) 1–9.

[64] B. Rajamani, J. Kim, A hybrid-filter approach to turbulence simulation, Flow, Turbulence and Combustion 85 (2010) 1–21.

[65] A. Fadai-Ghotbi, C. Friess, R. Manceau, J. Borée, A seamless hybrid RANS-LES model based on transport equations for the subgrid stresses and elliptic blending, Physics of Fluids 22 (2010) 055104.

[66] M. Sánchez-Rocha, S. Menon, An order-of-magnitude approximation for the hybrid terms in the compressible hybrid RANS/LES governing equations, Journal of Turbulence 12 (2011) 1–22.

[67] S. S. Girimaji, R. Sreenivasan, E. Jeong, PANS turbulence model for seamless transition between RANS, LES: Fixed-point analysis and preliminary results, in: FEDSM2003-45336, Proceedings of ASME FEDSM, vol. 3, 13–16, 2003.

[68] S. Lakshmipathy, S. Girimaji, Extension of Boussinesq turbulence constitutive relation for bridging methods, Journal of Turbulence 8 (2007) 1–21.

[69] A. Frendi, A. Tosh, S. Girimaji, Flow past a backward-facing step: Comparison of PANS, DES and URANS results with experiments, International Journal for Computational Methods in Engineering Science and Mechanics 8 (2007) 23–38.

[70] B. Basara, S. Krajnović, S. Girimaji, PANS vs. LES for computations of the flow around a 3D bluff body, in: 7th International ERCOFTAC

Symposium on Engineering Turbulence Modelling and Measurements, Limassol, Cyprus, 2008.

[71] S. Lakshmipathy, S. Girimaji, Partially averaged Navier–Stokes (PANS) method for turbulence simulations: Flow past a circular cylinder, Journal of Fluids Engineering 132 (2010) 121202.

[72] E. Jeong, S. Girimaji, Partially averaged Navier–Stokes (PANS) method for turbulence simulations: Flow past a square cylinder, Journal of Fluids Engineering 132 (2010) 121203.

[73] B. Basara, S. Krajnović, S. Girimaji, PANS methodology applied to elliptic-relaxation based eddy viscosity transport model, in: Proceedings of Turbulence and Interactions 2009 Conference, vol. NNFM 110, Springer, 63–69, 2010.

[74] B. Huang, G. Wang, Partially averaged Navier-Stokes method for time-dependent turbulent cavitating flows, Journal of Hydrodynamics, Ser. B 23 (2011) 26–33.

[75] H. Gopalan, S. Heinz, M. Stöllinger, Simulation of turbulent channel flow using a linear and nonlinear realizable unified RANS-LES model, in: 49th AIAA Aerospace Sciences Meeting and Exhibit, Orlando, FL, AIAA Paper 11–752, 2011.

[76] H. Gopalan, C. Zemtsop, S. Heinz, M. Stöllinger, Investigation of vortex breakdown and scalar mixing in swirling turbulent jet flows using unified LES-RANS models, in: 49th AIAA Aerospace Sciences Meeting and Exhibit, Orlando, FL, AIAA Paper 11–768, 2011.

[77] C. De Langhe, B. Merci, E. Dick, Application of a RG hybrid RANS/LES model to swirling confined turbulent jets, Journal of Turbulence 7 (2006) 1–19.

[78] C. De Langhe, J. Bigda, K. Lodefier, E. Dick, One-equation RG hybrid RANS/LES computation of a turbulent impinging jet, Journal of Turbulence 9 (2008) 1–19.

[79] S. Heinz, Molecular to fluid dynamics: The consequences of stochastic molecular motion, Physical Review E 70 (2004) 036308:1–11.

[80] B. Vreman, B. Geurts, H. Kuerten, Realizability conditions for the turbulent stress tensor in large-eddy simulation, Journal of Fluid Mechanics 278 (1994) 351–362.

[81] P. Durbin, C. Speziale, Realizability of second-moment closure via stochastic analysis, Journal of Fluid Mechanics 280 (1994) 395–407.

[82] U. Schumann, Realizability of Reynolds-stress turbulence models, Physics of Fluids 20 (1977) 721–725.

[83] S. Heinz, Realizability of dynamic subgrid-scale stress models via stochastic analysis, Monte Carlo Methods and Applications 14 (2008) 311–329.

[84] S. Heinz, Mathematical Modeling, Springer-Verlag, Heidelberg, Dordrecht, London, New York, 1st edn., 2011.

[85] J. Bredberg, S. Peng, L. Davidson, An improved k-ω turbulence model applied to recirculating flows, International Journal of Heat and Fluid Flow 23 (2002) 731–743.

[86] OpenFOAM documentation (www.openfoam.org), Tech. Rep., 2009.

[87] J. Bredberg, On two equation eddy-viscosity models, Chalmers University, Göteborg, Internal Report 1 (8) (2001) 1–41.

[88] L. Kleiser, U. Schumann, Treatment of incompressibility and boundary conditions in 3-D numerical spectral simulations of plane channel flows, in: Conference on Numerical Methods in Fluid Mechanics, 3rd, Cologne, West Germany, 165–173, 1980.

[89] J. Gibson, ChannelFlow Manual (www.channelflow.org), 2008.

[90] R. D. Moser, J. Kim, N. N. Mansour, Direct numerical simulation of turbulent channel flow up to Re_τ= 590, Physics of Fluids 11 (1999) 943–945.

[91] R. Issa, Solution of the implicitly discretised fluid flow equations by operator-splitting, Journal of Computational Physics 62 (1986) 40–65.

[92] M. Germano, U. Piomelli, P. Moin, W. H. Cabot, A dynamic subgrid-scale eddy viscosity model, Physics of Fluids A: Fluid Dynamics 3 (7) (1991) 1760–1765.

[93] U. Piomelli, High Reynolds number calculations using the dynamic subgrid-scale stress model, Physics of Fluids A: Fluid Dynamics 5 (6) (1993) 1484–1490.

[94] S. Ghosal, T. S. Lund, P. Moin, K. Akselvoll, A dynamic localization model for large-eddy simulation of turbulent flows, Journal of Fluid Mechanics 286 (1995) 229–255.

[95] K. Abe, A hybrid LES/RANS approach using an anisotropy-resolving algebraic turbulence model, International Journal of Heat and Fluid Flow 26 (2005) 204–222.

[96] A. Scotti, C. Meneveau, D. Lilly, Generalized Smagorinsky model for anisotropic grids, Physics of Fluids A: Fluid Dynamics 5 (1993) 2306–2308.

[97] C. Fureby, G. Tabor, Mathematical and physical constraints on Large-Eddy Simulations, Theoretical and Computational Fluid Dynamics 9 (1997) 85–102.

[98] S. Pope, Self-conditioned fields for large-eddy simulations of turbulent flows, Journal of Fluid Mechanics 652 (2010) 139–169.

[99] S. Hoyas, J. Jiménez, Scaling of the velocity fluctuations in turbulent channels up to Re_τ=2003, Physics of Fluids 18 (2006) 011702:1–4.

[100] H. Reichardt, Vollständige Darstellung der turbulenten Geschwindigkeitsverteilung in glatten Leitungen, ZAMM - Journal of Applied Mathematics and Mechanics 31 (2006) 208–219.

[101] J. Gullbrand, F. K. Chow, The effect of numerical errors and turbulence models in large-eddy simulations of channel flow, with and without explicit filtering, Journal of Fluid Mechanics 495 (2003) 323–341.

[102] R. Dean, Reynolds number dependence of skin friction and other bulk flow variables in two-dimensional rectangular duct flow, Journal of Fluids Engineering 100 (1978) 215–223.

[103] S. Heinz, H. Gopalan, Realizable versus non-realizable dynamic subgrid-scale stress models, Physics of Fluids 24 (11) (2012) 115105/1–23.

[104] M. Wolfshtein, The velocity and temperature distribution in one-dimensional flow with turbulence augmentation and pressure gradient, International Journal of Heat and Mass Transfer 12 (1969) 301–318.

[105] C. D. Langhe, J. Bigda, K. Lodefier, E. Dick, One-equation RG hybrid RANS/LES computation of a turbulent impinging jet, Journal of Turbulence 9 (16) (2008) 1–19.

[106] P. G. Tucker, Novel MILES computations for jet flows and noise, International Journal of Heat and Fluid Flow 25 (4) (2004) 625–635.

[107] C. D. Langhe, B. Merci, E. Dick, Application of a RG hybrid RANS/LES model to swirling confined turbulent jets, Journal of Turbulence 7 (56) (2006) 1–19.

Re$_\tau$	$Re = U_b L_y/\nu$	Domain size
180	5640	$4/3\pi * 2 * 4\pi$
395	13600	$2\pi * 2 * \pi$
590	21700	$2\pi * 2 * \pi$
950	37300	$8\pi * 2 * 3\pi$
2000	90000	$8\pi * 2 * 3\pi$
5000	246500	$8\pi * 2 * 3\pi$
10000	542000	$8\pi * 2 * 3\pi$

Table 1: Domain sizes for the friction Reynolds number cases considered. The domain sizes are chosen to match DNS. For the $Re_\tau = 180 - 590$ cases, the domain sizes were taken from Moser et al. [90]. For $Re_\tau = 950$ and $Re_\tau = 2000$, the domain sizes were taken from Hoyas and Jiménez [99]. The domain sizes for the higher Reynolds number cases were set equal to the $Re_\tau = 2000$ case.

Number	Grid Name	Grid size	Δx^+	Δz^+	Δy^+(min-max)
1.	DNS - F	$128 \times 193 \times 96$	20	13	0.029 - 4.81
2.	DNS - R	$64 \times 193 \times 48$	40	26	0.029 - 4.81
3.	DNS - C	$32 \times 193 \times 24$	80	52	0.029 - 4.81
4.	DNS - RANS	$8 \times 193 \times 4$	320	312	0.029 - 4.81
5.	RANS	$2 \times 64 \times 2$	1280	624	1.55 - 15.23
6.	VVVCLES	$4 \times 64 \times 4$	640	312	1.55 - 15.23
7.	VVCLES	$8 \times 64 \times 8$	320	156	1.55 - 15.23
8.	VCLES	$16 \times 64 \times 16$	160	78	1.55 - 15.23
9.	CLES	$32 \times 64 \times 32$	80	39	1.55 - 15.23
10.	LES	$64 \times 64 \times 64$	40	19.5	1.55 - 15.23
11.	FLES	$64 \times 100 \times 64$	40	19.5	0.45 - 12.45
12.	VFLES	$128 \times 150 \times 64$	245	245	1.9-270

Table 2: Grid nomenclature. The first four grids are used for *a priori* analyses: F, R, and C refer to fine, regular, and coarse LES grids, respectively, and RANS refers to a RANS grid. The remaining grids are used for *a posteriori* analyses (unified simulations). FLES refers to a fine LES grid, and VFLES refers to a very fine LES grid. The notation VVVC, VVC and VC refers to very very very coarse, very very coarse, and very coarse LES grids. The first eleven normalized $\Delta x^+, \Delta z^+, \Delta y^+$ values apply to the $Re_\tau = 395$ case, the last values apply to the $Re_\tau = 5000$ case.

Grid	I_1 Violation		I_2 Violation		I_3 Violation	
	Number of Points	Percent	Number of Points	Percent	Number of Points	Percent
RANS	0	0	0	0	0	0
VVVCLES	0	0	0	0	0	0
VVCLES	0	0	0	0	0	0
VCLES	7	0.042	18	0.11	16	0.098
CLES	13	0.02	47	0.072	51	0.078
LES	0	0	0	0	0	0
FLES	0	0	0	0	0	0
VFLES	0	0	0	0	0	0

Table 3: Realizability analysis of the linear unified stress tensor for the $Re_\tau = 395$ case. I_1, I_2, and I_3 refer to the three principal invariants of the turbulent stress tensor (see Sect. 8.1). The grids considered are defined in Table 1. At a given grid point, a violation refers to the occurrence of a negative value of an invariant.

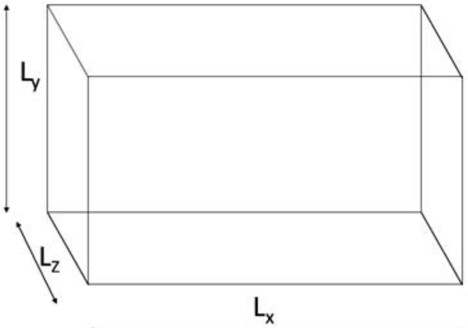

Figure 1: Problem setup: The domain size is chosen according to the Reynolds number considered.

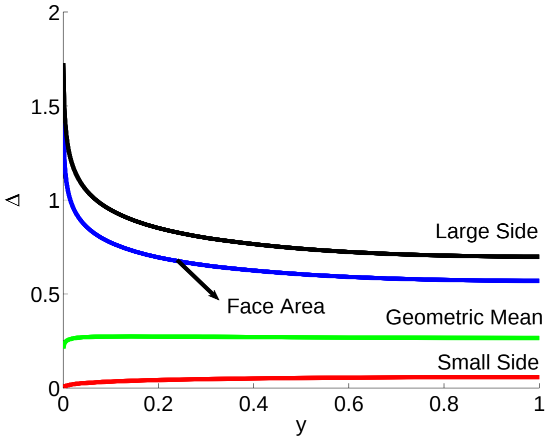

Figure 2: The variation of the filter width Δ along the wall-normal direction y for the four filter width definitions.

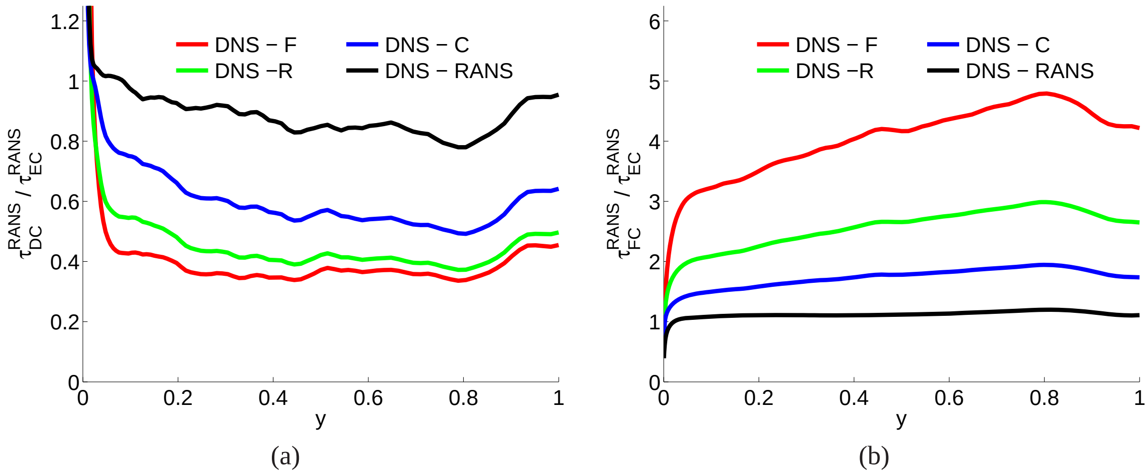

(a) (b)

Figure 3: Ratio of time scales in the DC and FC approach to the exact RANS time scale obtained from *a priori* analyses: (a) dynamic coupling, and (b) fixed coupling.

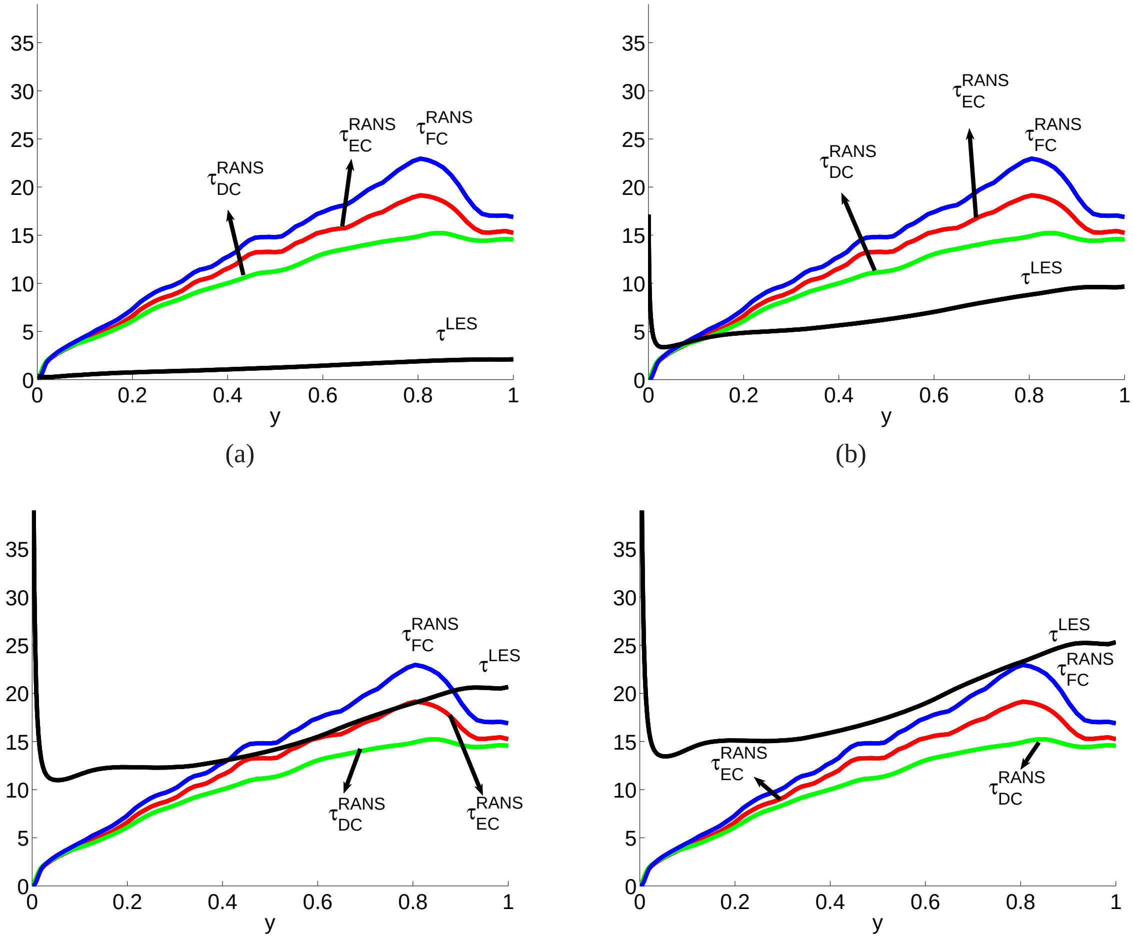

(a)

(b)

(c)

(d)

Figure 4: *A priori* analysis results for RANS and LES time scales obtained for the EC, DC, and FC coupling approaches on the DNS-RANS grid. The following filter width definitions are applied: (a) Small side filter, (b) Geometric mean filter, (c) Face area filter, and (d) Large side filter.

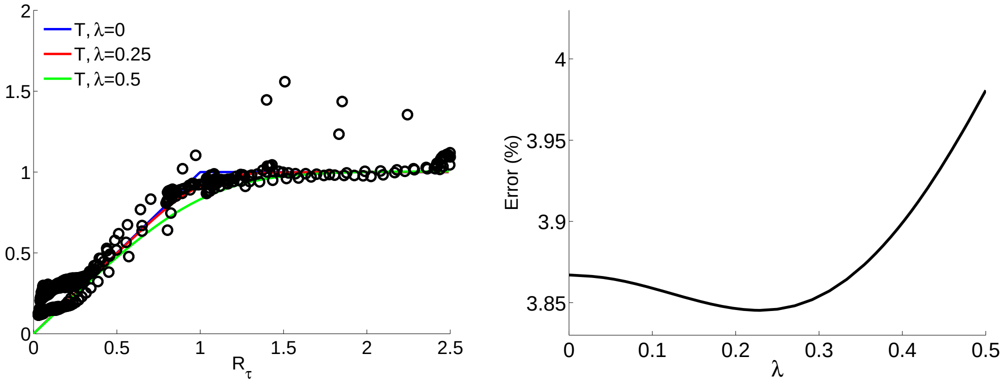

(a) (b)

Figure 5: Transfer function in the EC approach: (a) The exact transfer function (28) obtained from DNS is shown by dots, and the model transfer function (29) is shown by lines for three λ values; (b) The error (30) between the exact transfer function and the model transfer function using different λ values.

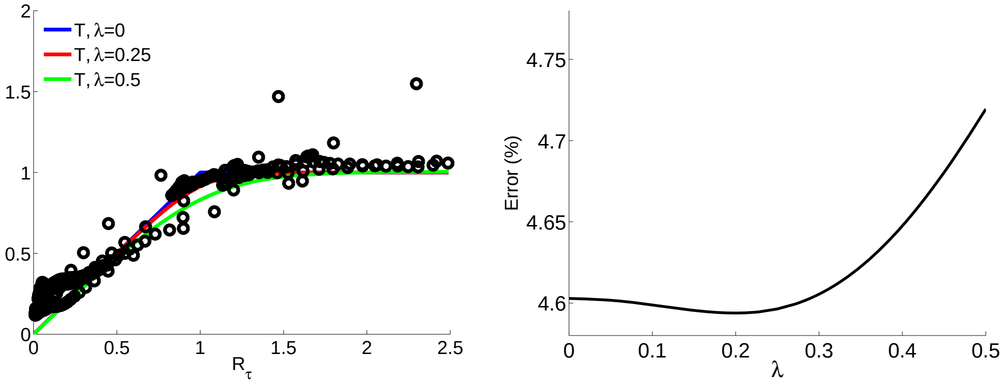

(a) (b)

Figure 6: The DC coupling approach results in correspondence to Fig. 5.

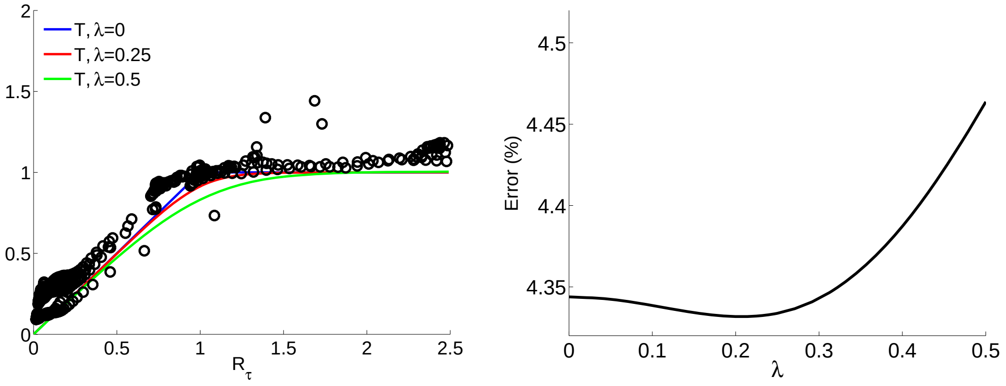

(a) (b)

Figure 7: The FC coupling approach results in correspondence to Fig. 5.

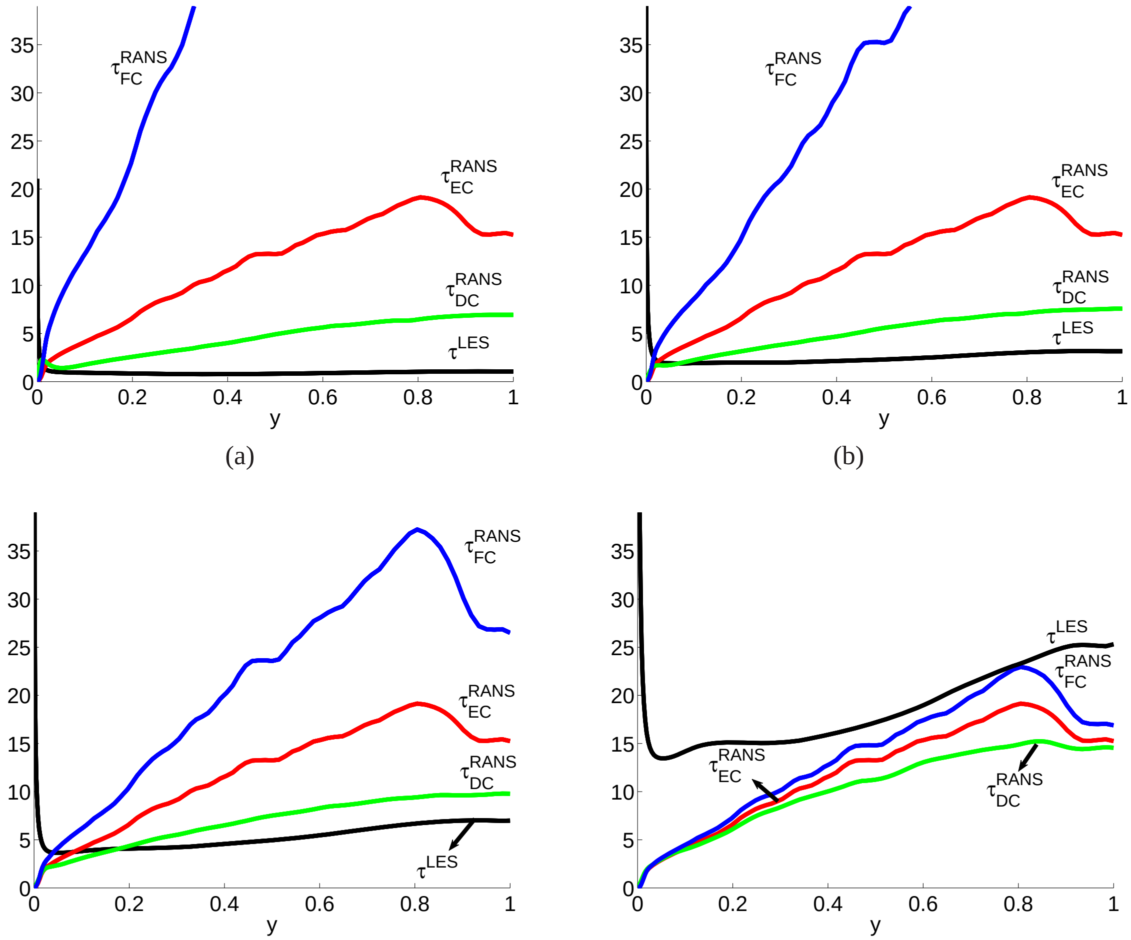

(a) (b) (c) (d)

Figure 8: *A priori* analysis results for RANS and LES time scales obtained for the EC, DC, and FC coupling approaches on different grids: (a) DNS - F grid, (b) DNS - R grid, (c) DNS - C grid, and (d) DNS - RANS grid.

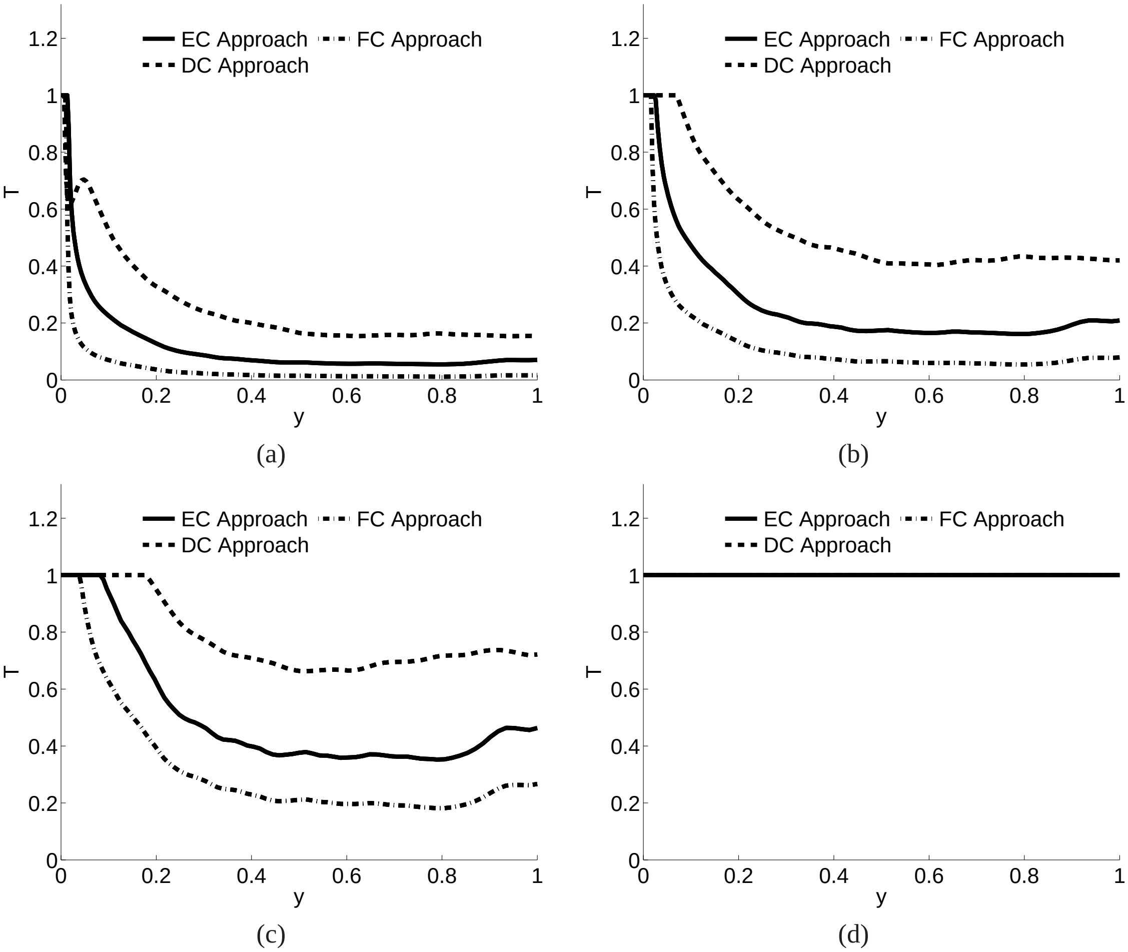

(a) (b) (c) (d)

Figure 9: *A priori* analysis results for the transfer function obtained for the EC, DC, and FC coupling approaches on different grids: (a) DNS - F grid, (b) DNS - R grid, (c) DNS - C grid, and (d) DNS - RANS grid.

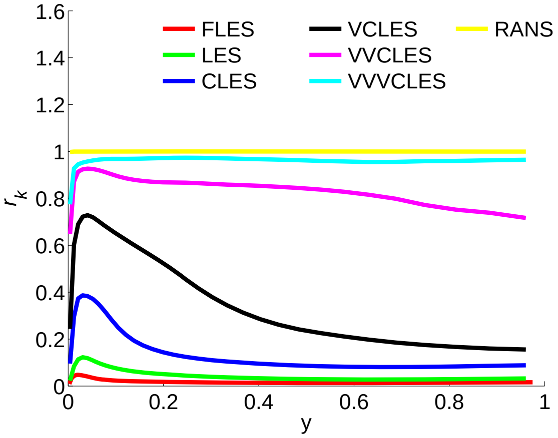

Figure 10: The ratio $r_k = k/(k + k_{res})$ of the modeled turbulent kinetic energy k to the total turbulent kinetic energy along the wall-normal direction y obtained from unified simulations on different grids. Here, k_{res} refers to the resolved turbulent kinetic energy.

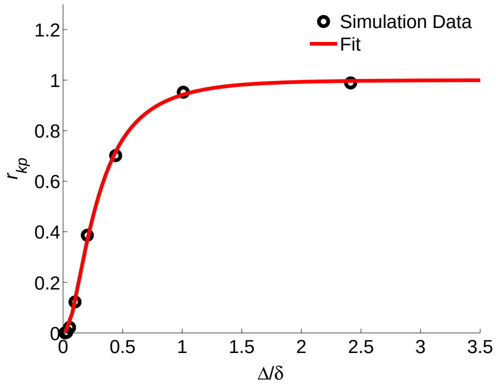

Figure 11: The dots show the peak value r_{kp} of the r_k curves given in Fig. 10 in dependence on the grid applied (Δ/δ). The line shows Eq. 31.

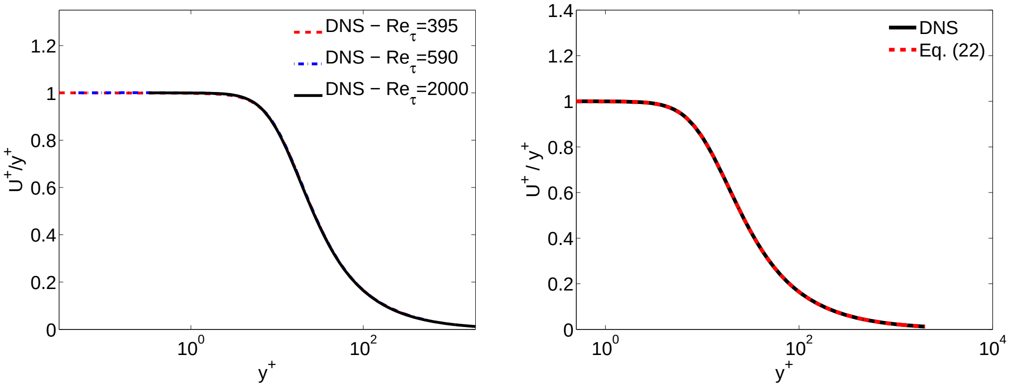

(a) (b)

Figure 12: (a) U^+/y^+ obtained from DNS at different friction Reynolds numbers Re_τ along the dimensionless wall distance y^+; (b) DNS data for the $Re_\tau = 2000$ case and Eq. (34).

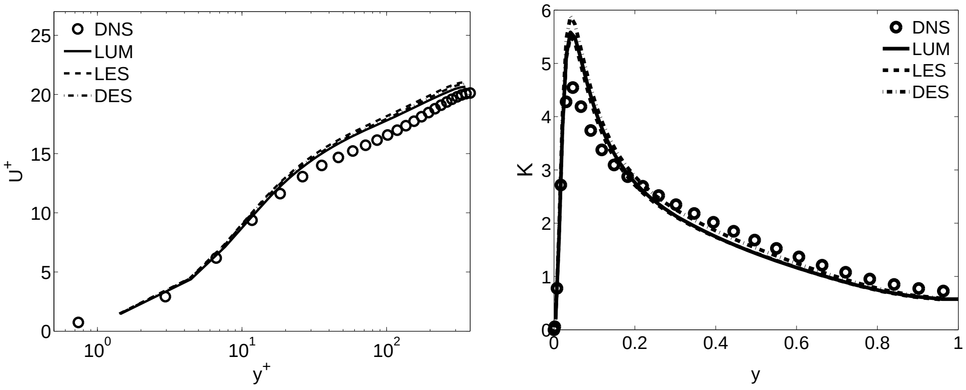

(a) (b)

Figure 13: Predictions obtained by the LUM, pure LES, DES, and DNS for $Re_\tau = 395$ on the LES grid: (a) the normalized mean streamwise velocity; (b) the normalized total turbulent kinetic energy $K = (k_{res} + k)/u_\tau^2$, where k_{res} refers to the resolved kinetic energy.

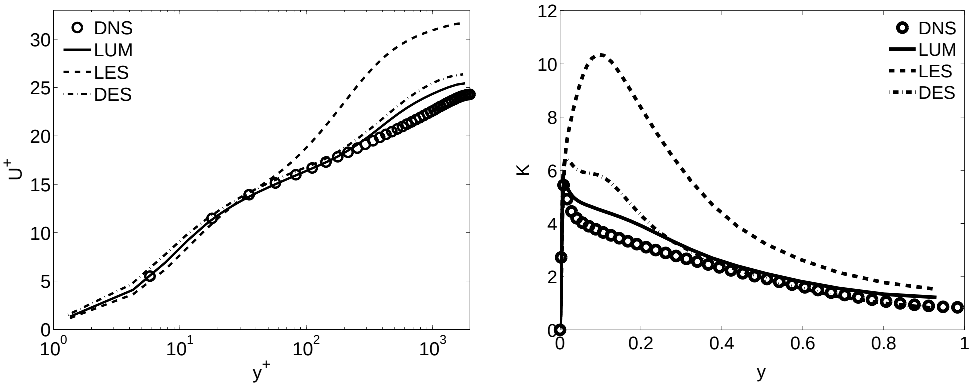

(a) (b)

Figure 14: The same comparisons as in Fig. 13 for $Re_\tau = 2000$.

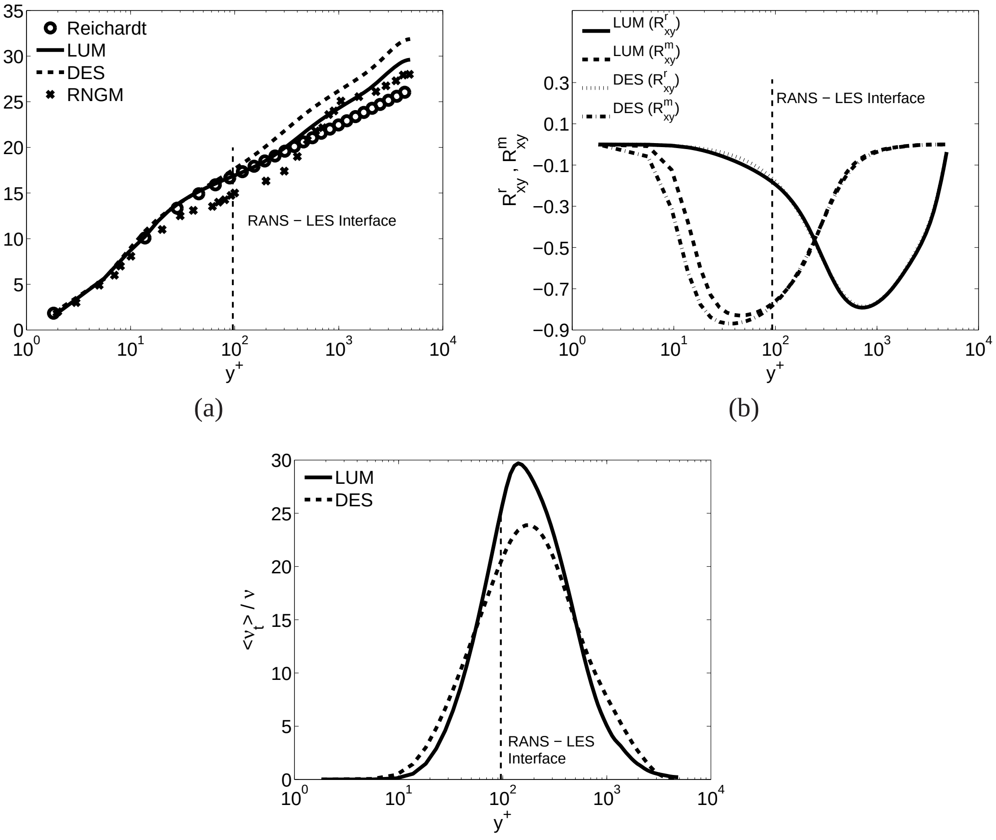

(a) (b)

(c)

Figure 15: Channel flow at $Re_\tau = 5000$: (a) Comparison of the mean streamwise velocity obtained by the LUM, DES, and RNGM with the Reichardt profile (34); (b) Comparison of the modeled (denoted by m) and resolved shear stress (denoted by r) obtained by the LUM and DES; (c) Comparison of the turbulent viscosity obtained by the LUM and DES. The vertical solid line refers to the RANS-LES interface location.

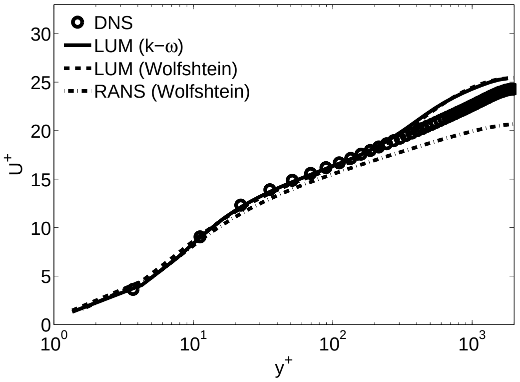

Figure 16: Channel flow at $Re_\tau = 2000$: Comparison of the mean streamwise velocity obtained by DNS, Wolfshtein's model in pure RANS mode, the unified model combined with the $k - \omega$ model, and the unified model combined with Wolfshtein's model.

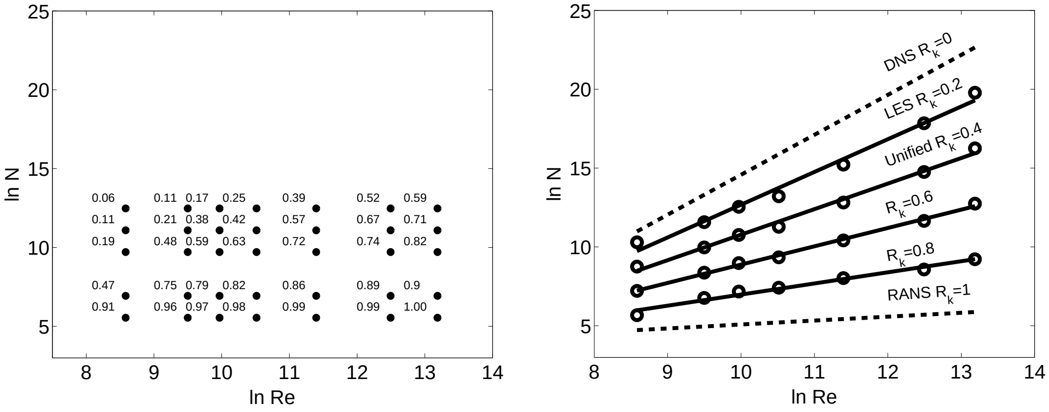

(a) (b)

Figure 17: The dependence of the number N of grid points on the Reynolds number Re: (a) simulation data (the corresponding R_k value is given next to the dot); (b) interpolated data (circles) compared with the implications of Eq. (40) (solid and dashed lines). The interpolated data were obtained by using the data given in (a) for calculating the values of N at the values $R_k = 0.2, 0.4, 0.6,$ and 0.8.

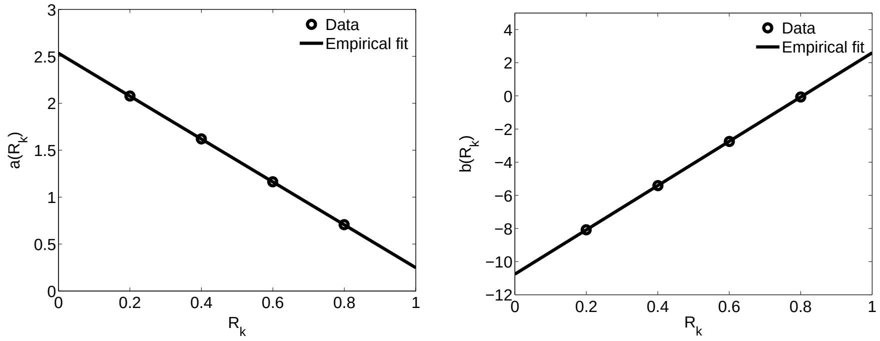

(a) (b)

Figure 18: The variations $a(R_k)$ and $b(R_k)$ of the model parameters in Eq. (39) with R_k are shown in (a) and (b), respectively. The dots represent interpolated data that follow from the data shown shown in Fig. 17b. The lines represent the linear interpolations $a(R_k) = 2.53 - 2.29R_k$ and $b(R_k) = 13.36R_k - 10.76$, respectively.

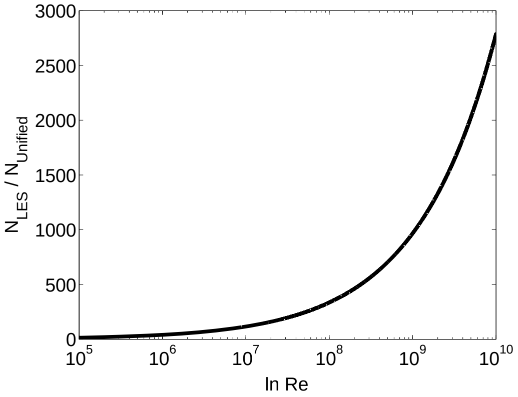

Figure 19: The LES to unified cost ratio given by Eq. (41) as a function of Reynolds number Re.